

Long term variation of the solar diurnal anisotropy of galactic cosmic rays observed with the Nagoya multi-directional muon detector

K. Munakata, M. Kozai, C. Kato

Physics Department, Shinshu University, Matsumoto, Nagano 390-8621, Japan

kmuna00@shinshu-u.ac.jp

and

J. Kóta

Lunar and Planetary Laboratory, University of Arizona, Tucson, AZ 87721, USA

Received _____; accepted _____

to be submitted for the regular issue of the Astrophysical Journal

ABSTRACT

We analyze the three dimensional anisotropy of the galactic cosmic ray (GCR) intensities observed independently with a muon detector (MD) at Nagoya in Japan and neutron monitors over four solar activity cycles. We clearly see the phase of the free-space diurnal anisotropy shifting toward earlier hours around solar activity minima in $A > 0$ epochs, due to the reduced anisotropy component parallel to the mean magnetic field. This component is consistent with a rigidity independent spectrum, while the perpendicular anisotropy component increases with GCR rigidity. We suggest that this harder spectrum of the perpendicular component is due to contribution from the drift streaming. We find that the bidirectional latitudinal density gradient is positive in $A > 0$ epoch, while it is negative in $A < 0$ epoch, in accord with the drift model prediction. The radial density gradient of GCRs, on the other hand, varies with ~ 11 -year cycle with maxima (minima) in solar maximum (minimum) periods, but we find no significant difference between the radial gradients in $A > 0$ and $A < 0$ epochs. The corresponding parallel mean free path is larger in $A < 0$ than in $A > 0$. We also find, however, that parallel mean free path (radial gradient) appears to persistently increase (decreasing) in the last three cycles of weakening solar activity. We suggest that simple differences between these parameters in $A > 0$ and $A < 0$ epochs are seriously biased by these long-term trends.

Subject headings: Sun: heliosphere, Sun: magnetic fields, methods: data analysis, cosmic rays, cosmic ray anisotropy

1. Introduction

The solar wind is a supersonic plasma blowing radially outward from the sun toward a vast space filled by cold and thin interstellar plasma. The global structure of the region called the “heliosphere”, which is a region dominated by the solar wind plasma and the solar magnetic field, is of great interest for both solar- and astrophysicists. The Interplanetary Magnetic Field (IMF) is the term representing the solar magnetic field carried outward by the solar wind into the heliosphere as magnetic field lines from the Sun are dragged along by the highly conductive solar wind plasma (Parker 1958). Because of the dominant dipole component of the solar magnetic field, the IMF is divided into two magnetic sectors in the northern and southern hemisphere separated by the Heliospheric Current Sheet (HCS) which develops into a “wavy” three dimensional structure. The inclination of the magnetic dipole from the rotation axis increases with increasing the solar activity and reverses during the solar activity maximum epoch when the inclination becomes maximum. The Sun has a strong and complex magnetic field, and the physical properties of the heliosphere is directly connected to the properties of the magnetic field varying with a period of about 11 years.

Temporal variations in the inner heliosphere can be deduced from the ground-based observations of the high-energy Galactic Cosmic Rays (GCRs). GCRs are high-energy nuclei (mostly protons) accelerated in our galaxy and continuously arriving at the earth after traveling through the heliosphere. After entering the heliosphere, GCRs interact with the IMF being carried outward by the solar wind. The interaction with the large-scale ordered field causes the gradient- and curvature-drift motions of GCRs in the heliosphere, while the interaction with the irregular (or disordered) field component results in the pitch angle scattering of GCRs. The scattering by the magnetic irregularities embedded in the expanding solar wind causes the deceleration (called the adiabatic cooling) and also causes an outward convection which leads to lower GCR intensities closer to the Sun. The resulting

positive radial gradient of GCRs produces an inward diffusion, flowing preferentially along the ordered IMF lines. A steady state distribution is realized when the inward diffusion is balanced with the outward convection. The GCR intensity measured at the Earth changes with various time scales. The solar cycle variation of the solar wind parameters, such as the solar wind velocity, the magnitude and orientation of the IMF, the tilt angle of the HCS and the mean free path of the pitch angle scattering of GCRs in the turbulent magnetic field, alters the spatial distribution of GCR density in the heliosphere. The drift model of GCR transport predicts a bi-directional latitudinal gradient pointing in opposite directions on the opposite sides of the HCS if the HCS is flat (Jokipii & Kopriva 1979). The predicted spatial distribution of the GCR density has a minimum along the HCS in the “positive” polarity period of the solar polar magnetic field (also referred as $A > 0$ epoch), when the IMF directs away from (toward) the Sun in the northern (southern) hemisphere, while the distribution has the local maximum on the HCS in the “negative” period ($A < 0$ epoch) with the opposite field orientation in each hemisphere. The field orientation reverses every 11 years around the maximum period of the solar activity. A tilted current sheet introduces modifications around the wavy HCS. For example the intensity minimum (for $A > 0$) will not be right at the HCS, but the general tendencies in the sense of the latitudinal gradient remain the same as outlined above (Jokipii & Kóta 1982).

The variation of the spatial distribution of GCR density causes the variation of the directional anisotropy of the GCR intensity measured at the Earth. One such variation is the 22-year variation of the solar diurnal anisotropy in which the phase (or the local solar time of maximum intensity) of the anisotropy shifts towards earlier hours around every $A > 0$ solar minima (Thambyahpillai & Elliot 1953; Forbush 1967; Ahluwalia 1988; Bieber & Chen 1991, and references therein). By analyzing the anisotropy observed with neutron monitors (NMs) in 1968-1988, Chen & Bieber (1993) (hereafter referred as Paper I) revealed that the observed phase-shift of the diurnal anisotropy is due to the decrease of

the diffusion streaming parallel to the IMF in $A > 0$ solar minima. The parallel diffusion streaming is proportional to the radial gradient (G_r) of GCR density multiplied by the parallel mean free path (λ_{\parallel}) of the pitch angle scattering. The simple drift model predicts smaller G_r in $A > 0$ epoch than in $A < 0$ epoch, if the diffusion coefficients are same in both epochs (Kóta & Jokipii 1983). Finding a significant 11-year solar cycle variation but no clear 22-year variation in the observed G_r , however, Paper I suggested that the smaller parallel streaming in the $A > 0$ solar minimum period was caused by the smaller λ_{\parallel} , possibly due to the magnetic helicity effect in the turbulent magnetic field (Paper I; Bieber & Pomerantz 1986; Bieber et al. 1987).

The GCR anisotropy (or the streaming) vector in three dimensions (3D) consists of three components, two lying in the ecliptic plane and the other pointing normal to the ecliptic plane. The two ecliptic components, parallel and perpendicular to the IMF, are derived from the amplitude and phase of the solar diurnal anisotropy corrected for the contribution from the radial solar wind convection. Paper I analyzed the diurnal anisotropy in free space, corrected for the geomagnetic deflection of GCR orbits, by assuming a power law type ($\propto p^{\gamma}$) dependence of the anisotropy amplitude on the GCR rigidity (p) with the spectral index (γ) and the upper limiting rigidity (P_u) fixed at 0 and 100 GV, respectively. The zero spectral index of the diurnal anisotropy has been assumed in many analyses based on the original convection-diffusion picture of the GCR transport in which the stationary GCR distribution in the heliosphere results from the inward diffusion balancing with the outward convection by the solar wind which is independent of the rigidity (Parker 1965; Gleeson & Axford 1967; Gleeson 1969). The upper limiting rigidity (P_u) set at 100 GV was also a reasonable assumption for the analysis of NM data alone, because P_u representing the break-down rigidity of the diffusion picture is expected to be much higher than the median primary rigidity to which the NMs used in Paper I respond. Munakata et al. (1997) assumed $\gamma = 0$ but treated P_u as a free parameter in their analyses of the diurnal anisotropy

observed with multi-directional muon detectors (MDs) which have median responses to GCRs with higher rigidity than NMs. They found P_u changing between 100 and 300 GV in a clear correlation with the solar activity (Munakata et al. 2002). Hall et al. (1997) treated both γ and P_u as free parameters in their analyses of the NM and MD data and reported the temporal variation of each parameter in solar activity and solar magnetic cycles.

All these works take account of the rigidity dependence of the amplitude varying as a function of time, but they still assume that the phase is independent of rigidity. In other words, they assumed a common rigidity spectrum for two ecliptic components, parallel and perpendicular to the IMF. Bieber & Chen (1991) (hereafter referred as Paper II), on the other hand, also reported that the magnitude of the observed phase variation in $A > 0$ solar minimum increases with GCR rigidity (Agrawal 1983). This rigidity dependent feature of the observed phase variation cannot be reproduced properly, as long as the rigidity spectrum common for two ecliptic components is assumed. This observed feature has been confirmed by other papers (e.g. Oh et al. 2010), but its physical origin is still left unknown.

The third component of the anisotropy, that is, the north-south (NS) anisotropy normal to the ecliptic plane has been derived also from NM and MD data in a couple of different ways. Bieber & Pomerantz (1986) and Paper I derived this anisotropy from the difference between count rates in a pair of NMs which are located near the north and south geomagnetic poles and observing intensities of GCRs arriving from the north and south pole orientations, respectively. They found a ~ 10 -year cycle variation in this component anisotropy which implied the radial gradient (G_r) of GCR density changing in correlation with the solar activity, while they found no significant difference of G_r in $A > 0$ and $A < 0$ epochs in a contradiction with the simple drift model prediction. Due to 23.4° inclination of Earth's rotation axis from the ecliptic normal, the NS anisotropy normal to the ecliptic plane can be also observed as a diurnal variation of count rate in the sidereal time with

the maximum phase at $\sim 18:00$ local sidereal time (Swinson 1969). Yasue (1980) analyzed this sidereal diurnal variation observed by NMs and MDs during 5 years between 1969 and 1973 and found that observations were reproduced best by the average rigidity spectrum with $\gamma = 0.3$ and $P_u = 200$ GV. This was the first experimental indication that the rigidity spectrum of the anisotropy has a positive spectral index. Hall et al. (1994) also applied the same method to NM and MD data observed between 1957 and 1985 and found the average spectrum with $\gamma = 0.5$ and $P_u = 400$ GV, again with a positive γ . This suggested that each of two ecliptic components may also have a spectrum with non-zero γ .

A possible drawback of deriving the NS anisotropy from the sidereal diurnal variation is that the expected amplitude of the sidereal diurnal variation (~ 0.03 %) is approximately an order of magnitude smaller than the solar diurnal variation (~ 0.3 %). The small signal in the sidereal time can be easily influenced by the solar diurnal anisotropy changing in a year. Another difficulty is that one can obtain only the yearly mean anisotropy. This is because of the fact that the influence from the solar diurnal variation, even if it is stationary through a year, can be eliminated in the sidereal time only when the diurnal variation is averaged over integral year(s). This makes it difficult to deduce reliable error of the yearly mean anisotropy. Mori & Nagashima (1979) proposed another way to derive the NS anisotropy from the “GG-component” of a multi-directional MD at Nagoya in Japan. The GG-component is a difference combination between intensities recorded in the north- and south-viewing directional channels designed to measure the NS anisotropy free from the atmospheric temperature effect (Nagashima et al. 1972). Laurenza & Storini (2003) showed that GG-component can be used for deriving reliable sector polarity of the IMF. By using a global network of four multi-directional MDs which are capable of observing the NS anisotropy on hourly basis, Okazaki et al. (2008) confirmed that the north-south anisotropy deduced from the GG-component is consistent with the anisotropy observed with the global network.

In the present paper, we extend the analysis by Paper I to the most recent period and derive the long-term variation of the modulation parameters from the 3D anisotropy observed during 44 years by the Nagoya multi-directional MD which has a median rigidity of 60 GV for primary GCRs. We also analyze the anisotropy observed during the same period by NMs which have the median response to 17 GV primary GCRs. We derive the NS anisotropy from the GG-component of the Nagoya MD. We particularly examine the rigidity dependences of each component of the anisotropy and each modulation parameter by comparing them derived from MD and NM data at 60 GV and 17 GV, respectively. We do not intend to determine each rigidity spectrum quantitatively by, for instance, calculating both γ and P_u as free parameters in best-fit calculation as a function of time. In such best-fit calculations, we often see a significant anti-correlation between the best-fit γ and P_u (Hall et al. 1994, 1997). A large P_u with a small (or negative) γ often returns similar χ^2 -value as a small P_u with large (or positive) γ does, increasing the systematic error of each best-fit value. We instead examine the rigidity spectrum qualitatively based on the ratio between parameters derived from NM and MD data with a common assumption of the spectrum with fixed values of $\gamma = 0$ and $P_u = 100$ GV, respectively, as done in Paper I. If the ratio is close to one, the spectrum is consistent with the assumption. If the ratio is significantly larger (smaller) than one, on the other hand, we can conclude that the spectrum is harder (softer) than the assumed one. In this way, we can make a qualitative but reliable examination of the rigidity dependence of each parameter. We will present quantitative analyses of the rigidity dependence elsewhere. It will be shown in the present paper that three components of the anisotropy have different rigidity dependence. This naturally explains the rigidity dependent feature of the observed phase variation mentioned above. We will also suggest that the different rigidity dependence for three anisotropy components are possibly due to the relative contribution from the drift (diamagnetic drift) which is different in each component.

The outline of this paper is as follows. In section 2, we describe the data analysis and results in detail. The conclusions and discussions are given in section 3. For readers' references, we also present our results in a numerical data table in Appendix A. In Appendix B, we show how the obtained results depend on the assumed value of P_u .

2. Data analyses and results

We derive the cosmic ray anisotropy in three dimensions by analyzing the pressure corrected hourly count rates recorded by a muon detector (MD) at Nagoya in Japan during 44 years between 1970 and 2013. Nagoya muon detector is multi-directional and capable of simultaneously monitoring intensities in 17 directional channels of viewing (see figure 1). It has been in operation since 1970 producing a continuous record of cosmic ray intensity over four decades and allowing us to analyze the long term variation of the anisotropy¹. Based on our own experience of the long-term observation using plastic scintillators and PMTs similar to Nagoya MD, we estimate that the absolute muon count rate by Nagoya MD has decreased $\sim 10\%$ or less in four decades due to the deterioration of detectors. The effect of this deterioration, however, should be negligibly small for the GCR anisotropy analyzed in this paper, because our analysis does not use the absolute count rate but the fractional deviation of the count rate from the daily or monthly mean, as shown later in this section. The median rigidity (P_m) of primary GCRs, calculated by utilizing the response function of the atmospheric muons to the primary particles (Murakami et al. 1979), ranges from 59.4 to 113.7 GV, and the statistical error of hourly count rate ranges between 0.06% and 0.28% (Okazaki et al. 2008). In this paper, we use 60 GV for the representative P_m of

¹Description and data of Nagoya MD are available at <http://www.stelab.nagoya-u.ac.jp/ste-www1/div3/muon/muon1.html>.

Nagoya MD. The response function has been first calculated for each element in GCRs and then averaged with the weight according to the observed elemental abundance of GCRs (Murakami et al. 1979).

We also derive the anisotropy by analyzing the data recorded during the same period by neutron monitors (NMs), Swarthmore/Newark, Alert/Thule and McMurdo, for each of which P_{ms} is 17 GV (Yasue et al. 1982). We use the data from Swarthmore/Newark to derive the diurnal anisotropy, while we derive the NS anisotropy from a pair of polar NMs at Thule in Greenland (or Alert in Canada) and McMurdo in Antarctica.² By comparing anisotropies derived from MD and NMs whose P_m differ by a factor of about 3.5 from each other, we discuss the rigidity dependence of the anisotropy and its long term variation. Table 1 summarizes the cosmic ray data analyzed in this paper.

In this section, we describe our analyses of Nagoya MD data, while we derive the anisotropy in free space from NMs in Table 1 following the analyses in Paper I and Paper II. For our analyses of NM data, therefore, readers can refer to those papers.

2.1. Elimination of short-term events and derivation of the observed diurnal variation

We begin our analyses with calculating the fractional deviation $\Delta I_j(t)$ of the pressure corrected hourly muon count rate $I_j(t)$ in the j -th directional channel of Nagoya MD ($j = 1, 2, \dots, 17$) at the universal time t from the 24-hours central moving average $\bar{I}_j^{24h}(t)$, as

$$\Delta I_j(t) = (I_j(t) - \bar{I}_j^{24h}(t)) / \bar{I}_j^{24h}(t) \quad (1)$$

²Description and data of NMs are available at <http://neutronm.bartol.udel.edu/> and <http://center.stelab.nagoya-u.ac.jp/WDCCR/>.

where

$$\bar{I}_j^{24\text{h}}(t) = \frac{1}{24} \sum_{t-12}^{t+11} I_j(t). \quad (2)$$

For the following analyses of the diurnal anisotropy, we use $\Delta I_j(t)$ in equation (1) instead of $I_j(t)$ itself to avoid the influence of the gradual intensity variation, such as day-to-day variation, to the diurnal variation. We then check the difference between the maximum and minimum values of $\Delta I_{NM}(t)$ for the McMurdo NM data in every day and exclude the day with the difference exceeding 2.0 % from further analyses to avoid the influence of large cosmic ray events such as the Forbush decreases. Total 777 days are excluded out of 16,071 days in 44 years between 1970 and 2013 in our analyses of MD and NM data. We confirmed that these excluded days include the majority of cosmic ray events reported so far (Cane et al. 1996; Jordan et al. 2011). From $\Delta I_j(t)$ in the remaining days, we obtain the monthly mean diurnal distribution, $d_j(t_k)$, of $\Delta I_j(t)$ as a function of the local solar time $t_k (k = 1, 2, \dots, 24)$ at the observation site, Nagoya in Japan.

We then deduce the diurnal variation of GCR intensity from the Fourier analysis of $d_j(t_k)$ described above, as

$$a_{1,j}^{1,\text{obs}} = \frac{1}{\pi} \sum_{k=1}^{24} d_j(t_k) \cos(\omega t_k) \quad (3a)$$

$$b_{1,j}^{1,\text{obs}} = \frac{1}{\pi} \sum_{k=1}^{24} d_j(t_k) \sin(\omega t_k) \quad (3b)$$

where $a_{1,j}^{1,\text{obs}}$ and $b_{1,j}^{1,\text{obs}}$ are the observed harmonic components of the monthly average diurnal variation and ω is $\pi/12$. In the following subsections, we use $a_{1,j}^{1,\text{obs}}$ and $b_{1,j}^{1,\text{obs}}$ for deriving the diurnal anisotropy at 60 GV in free space corrected for the geomagnetic effects by taking account of the energy response of each directional channel. We use $a_{1,j}^{1,\text{obs}}$ and $b_{1,j}^{1,\text{obs}}$ observed by Newark/Swarthmore NM during the same period for deriving the free space diurnal anisotropy at 17 GeV (see Paper II).

2.2. Correction for the Compton-Getting effect arising from the Earth's orbital motion around the Sun

The Earth's orbital motion around the Sun causes an apparent anisotropy due to the Compton-Getting (CG) effect (Compton & Getting 1935; Cutler & Groom 1986; Amenomori et al. 2004). The amplitude and phase of this apparent anisotropy in space are known to be independent of particle's rigidity p . Space harmonic components of this anisotropy, ξ_x^{CG} and ξ_y^{CG} in the Geocentric Solar Ecliptic coordinate system (GSE), are given, as

$$\xi_x^{\text{CG}} = 0, \quad (4a)$$

$$\xi_y^{\text{CG}} = -(2 + \Gamma)v_E/c \quad (4b)$$

where Γ is the power law index of the energy spectrum of GCRs, v_E is the Earth's velocity and c is the speed of light. We set Γ and v_E to be 2.7 and 30 km/s, respectively. Note that we define the anisotropy vector throughout this paper as a vector pointing toward a direction *from* which the highest GCR flux is measured; i.e., the anisotropy vector is oppositely directed to the GCR streaming vector.

The harmonic components of the diurnal variation expected from this effect for j -th directional channel of MD are then given, as

$$a_{1,j}^{1,\text{CG}} = c_{1,j}^{1,\text{CG}} \xi_x^{\text{CG(GEO)}} + s_{1,j}^{1,\text{CG}} \xi_y^{\text{CG(GEO)}} \quad (5a)$$

$$b_{1,j}^{1,\text{CG}} = -s_{1,j}^{1,\text{CG}} \xi_x^{\text{CG(GEO)}} + c_{1,j}^{1,\text{CG}} \xi_y^{\text{CG(GEO)}} \quad (5b)$$

where $\xi_x^{\text{CG(GEO)}}$ and $\xi_y^{\text{CG(GEO)}}$ are the space harmonic components of the CG anisotropy transformed to the Geographic coordinate system (GEO) and $c_{1,j}^{1,\text{CG}}$ and $s_{1,j}^{1,\text{CG}}$ are so-called the coupling coefficients relating the observed harmonic vector with the space harmonic vector and are calculated (Fujimoto et al. 1984), as

$$c_{1,j}^{1,\text{CG}} = \frac{1}{\bar{I}_j} \int_{p_{cj}}^{\infty} \int_{\Omega_j} \int_{S_j} Y \cdot G^{\text{CG}}(p) \cdot P_1^1(\cos \theta_{\text{or}}) \cdot \cos(\phi_{\text{or}} - \phi_{\text{st}}) dS d\Omega dp \quad (6a)$$

$$s_{1,j}^{1,\text{CG}} = \frac{1}{\bar{I}_j} \int_{p_{cj}}^{\infty} \int_{\Omega_j} \int_{S_j} Y \cdot G^{\text{CG}}(p) \cdot P_1^1(\cos \theta_{\text{or}}) \cdot \sin(\phi_{\text{or}} - \phi_{\text{st}}) dS d\Omega dp. \quad (6b)$$

In equations (6a) and (6b), \bar{I}_j is the average count rate in the j -th directional channel of muon detector, Y is the response function of the atmospheric muons to primary GCRs and p_{cj} is the cut-off rigidity below which Y is insignificant (Murakami et al. 1979). The response function Y gives the number of muons produced by primary particles of rigidity p and arriving at j -th directional channel with the zenith angle θ and azimuth angle ϕ . $P_1^1(x)$ is the semi-normalized spherical function $P_n^m(x)$ with $n = m = 1$ (Chapman & Bartels 1940). S_j and Ω_j are respectively the total area and solid angle of the j -th directional channel and dS and $d\Omega$ are those elements. ϕ_{st} is the geographic longitude of the detector site and θ_{or} and ϕ_{or} are respectively the geographic co-latitude and longitude defining the asymptotic direction outside the geomagnetic field of primary particles with p which produce muons with the incident direction (θ, ϕ) , as determined using a particle trajectory code (Lin et al. 1995). The integrals in equations (6a) and (6b) are over all rigidity values for which primary particles produce detectable muons and over all incident directions (θ, ϕ) for which muon can enter the j -th directional channel. In equations (6a) and (6b), G^{CG} is the rigidity spectrum of the Compton-Getting anisotropy and independent of p , as

$$G^{\text{CG}}(p) = 1. \quad (7)$$

Using equations (5a) and (5b) as an example, we briefly describe a physical implication of the coupling coefficients. The phase of the CG-anisotropy in space given in equations (4a) and (4b) is 270° in the GSE longitude or 06:00 hour in the local solar time. With the coupling coefficients $c_{1,j}^{1,\text{CG}}$ and $s_{1,j}^{1,\text{CG}}$ in equations (6a) and (6b) which are both positive for the vertical channel of Nagoya MD, we get $a_{1,j}^{1,\text{CG}}$ and $b_{1,j}^{1,\text{CG}}$ in equations (5a) and (5b) both positive for this channel, representing the phase of the observed anisotropy shifted to earlier hours from 06:00 hour in space due to the deflection of orbits of positively charged GCRs in the geomagnetic field. In case of $a_{1,j}^1$ and $b_{1,j}^1$ due to the unknown anisotropy, we can use

the coupling coefficients to correct the observed anisotropy for the geomagnetic deflection, by solving equations like (5a) and (5b) for the unknown anisotropy (ξ_x, ξ_y) in space.

As described below, we correct the observed diurnal variation for the CG effect by subtracting the expected harmonic components $a_{1,j}^{1,\text{CG}}$ and $b_{1,j}^{1,\text{CG}}$ in equations (5a) and (5b) from the observed components $a_{1,j}^{1,\text{obs}}$ and $b_{1,j}^{1,\text{obs}}$ in equations (3a) and (3b), respectively.

2.3. Derivation of the three dimensional anisotropy in free space

The three dimensional (3D) anisotropy of GCR intensity consists of three components, two lying in the ecliptic plane and the third pointing normal to the ecliptic plane. The ecliptic components are observed as the diurnal variation in solar time of GCR intensity recorded with a ground based detector, while the normal component is observed as the north-south (NS) anisotropy. In the following sub sections, we deduce the diurnal anisotropy and the NS anisotropy at 60 GV from Nagoya MD data, while we derive the anisotropy at 17 GV from NM data in Table 1.

2.3.1. Modeling harmonic components of the diurnal variation

The harmonic components $a_{1,j}^{1,\text{obs}}$ and $b_{1,j}^{1,\text{obs}}$ of the diurnal anisotropy observed by Nagoya MD are expressed in terms of the unknown harmonic components ξ_x^{GEO} and ξ_y^{GEO} representing the diurnal anisotropy in free-space in the Geographic coordinate system (GEO), as

$$a_{1,j}^1 = a_{1,j}^{1,\text{CG}} + c_{1,j}^1 \xi_x^{\text{GEO}} + s_{1,j}^1 \xi_y^{\text{GEO}} + a_{\text{com}} \quad (8a)$$

$$b_{1,j}^1 = b_{1,j}^{1,\text{CG}} - s_{1,j}^1 \xi_x^{\text{GEO}} + c_{1,j}^1 \xi_y^{\text{GEO}} + b_{\text{com}} \quad (8b)$$

where $c_{1,j}^1$ and $s_{1,j}^1$ are the coupling coefficients given by equations (6a) and (6b) with $G^{\text{CG}}(p)$ replaced with $G(p)$ for the unknown rigidity spectrum of the diurnal anisotropy. In equations (8a) and (8b), a_{com} and b_{com} are harmonic components of the diurnal variation arising from the atmospheric temperature effect on muon intensity which is assumed in this paper to be common for all directional channels as the first-order approximation. For $G(p)$, we assume in this paper,

$$\begin{aligned} G(p) &= 1 \text{ for } p \leq P_u \\ &= 0 \text{ for } p > P_u \end{aligned} \quad (9)$$

where P_u is the upper limiting rigidity of the anisotropy and set to be constant at 100 GV. This spectrum is used in Paper II for the analysis of NM data and we use the same spectrum for MD data as well. Results derived with different P_u are shown and discussed in Appendix B.

2.3.2. Deriving the diurnal anisotropy in free space

We deduce the best-fit parameters ξ_x^{GEO} , ξ_y^{GEO} , a_{com} and b_{com} in equations (8a) and (8b) that minimize the residual S , defined as

$$S = \sum_{j=1}^{17} \left\{ \left(a_{1,j}^{1,\text{obs}} - a_{1,j}^1 \right)^2 / \sigma_{a,j}^2 + \left(b_{1,j}^{1,\text{obs}} - b_{1,j}^1 \right)^2 / \sigma_{b,j}^2 \right\} \quad (10)$$

where $\sigma_{a,j}$ and $\sigma_{b,j}$ are errors of $a_{1,j}^{1,\text{obs}}$ and $b_{1,j}^{1,\text{obs}}$, respectively, and deduced from the dispersion of $\Delta I_j(t)$ used for calculating the monthly mean $d_j(t_k)$ at the local time t_k in equations (3a) and (3b). We perform this calculation for every month and calculate yearly mean values and errors of ξ_x^{GEO} , ξ_y^{GEO} , a_{com} and b_{com} from means and dispersions of 12 monthly values, respectively. Figure 2 displays sample comparisons between the best-fit and the observed yearly mean harmonic vectors for Nagoya MD in 2002 and 1976 when the

solar activity were close to the maximum and minimum, respectively. It is clear that the amplitude of the derived space harmonic vector indicated in each panel is significantly larger in 2002 than that in 1976 causing an “expansion” of the pattern drawn by lines connecting heads of harmonic vectors observed by 17 directional channels during the solar maximum period. It is also clear that the phase of the derived space harmonic vector is about 4 hours earlier in 1976 than in 2002, due to the 22-year variation of the diurnal anisotropy.

2.3.3. Identification of IMF sector and solar dipole magnetic field polarities

In order to calculate the diurnal anisotropy in each IMF sector, we identify the sector polarity (*toward* or *away*) of each day referring to the polarity of the Stanford Mean Magnetic Field of the Sun (WSO web-site at <http://wso.stanford.edu/>) with the date shifted 5 days later for a rough correction for the solar wind transit time between the Sun and the Earth. For the period prior to 1975 when the data are not available on the WSO web-site, we identify the polarity by the IMF data in the National Space Science Data Center’s “omnitape” (King 2005) following the analysis by Paper II. Because of serious gaps in the “omnitape” data particularly in 1980’s and 1990’s, we give it up to use the “omnitape” IMF data for an entire period of the present analysis. By analyzing a period when both the Stanford Mean Magnetic Field and the “omnitape” data are available, we confirmed that the daily sector polarities identified by these two methods are quite consistent with each other, giving the essentially same results from our cosmic ray data analyses.

We then calculate the average diurnal distribution, $d_j^T(t_k)$ ($d_j^A(t_k)$), for *toward* (*away*) days in every month. By using $d_j^T(t_k)$ ($d_j^A(t_k)$) for $d_j(t_k)$ in equations (3a) and (3b) and for the best-fit calculation described above, we obtain $\xi_x^{\text{GEO}(T)}$, $\xi_y^{\text{GEO}(T)}$, a_{com}^T and b_{com}^T ($\xi_x^{\text{GEO}(A)}$, $\xi_y^{\text{GEO}(A)}$, a_{com}^A and b_{com}^A) in *toward* (*away*) sector in every month. Monthly mean parameters

are then calculated by taking mean of *toward* and *away* values.

For the following discussions of yearly mean parameter, we also assign the polarity of the large-scale solar magnetic field for each year referring to the “Solar Polar Field Strength” available at the WSO web-site where the average polar field strength is given in every Carrington Rotation. We assign the polarity of a year as $A > 0$ ($A < 0$) when the average polar field in the year is positive pointing away from the Sun in the northern (southern) hemisphere. We regard a year as a period of the polarity reversal in progress when the year contains Carrington Rotations with the polar field pointing *away* or *toward* in both hemispheres. For a period prior to 1975 when the WSO data are unavailable, we follow the assignment by Paper I. The polarity of each year assigned by us is indicated in Table 2 in Appendix A.

Figure 3 displays temporal variations of the amplitude (upper panel) and phase (lower panel) of the yearly mean harmonic vector in free-space. Clearly seen in this figure is the phase in the lower panel showing a prominent 22-year variation, with minima occurring in 1976 and 1997 around $A > 0$ solar minima. This phase variation is about ~ 2 hours in NM data (open circles), while it is almost double (~ 4 hours) in MD data (solid circles). The amplitude of the diurnal anisotropy in the upper panel is smaller (larger) around the solar minimum (maximum) period in both the NM and MD data. Table 2 in Appendix A lists numerical data of best-fit parameters obtained for each year. As shown in figure 9 in Appendix A, the mean amplitude of the common vector ($a_{\text{com}}, b_{\text{com}}$) in equations (8a) and (8b), which is introduced to represent the atmospheric temperature effect, is small (0.039 ± 0.002 %), while the phase is almost stable around $\sim 06:00$ local time in an agreement with the average temperature effect reported from muon observations (e.g. Munakata et al. 1997). It is also seen in figure 9 that the common vector shows no notable long-term variations in correlation with the solar activity- or magnetic-cycle.

2.3.4. Derivation of the north-south anisotropy

We derive the north-south (NS) anisotropy perpendicular to the ecliptic plane at 60 GV from the Nagoya GG-component (see Paper II for the derivation of the north-south anisotropy from NM data). The GG-component is a difference combination between intensities recorded in the north- and south-viewing channels designed to represent the NS anisotropy free from the atmospheric temperature effect (Nagashima et al. 1972; Mori & Nagashima 1979). The GG-component is defined, as

$$GG(t) = \{r_{N2}(t) - r_{S2}(t)\} + \{r_{N2}(t) - r_{E2}(t)\} \quad (11)$$

where $r_{XX}(t)$ is the percent deviation of the pressure-corrected muon rate $I_{XX}(t)$ in the directional channel XX(= N2, S2, E2) from the monthly mean. We calculate GG^T and GG^A by averaging $GG(t)$ over *toward* and *away* days, respectively, according to the IMF sector polarity in every month and calculate the difference, ΔGG , as

$$\Delta GG = (GG^T - GG^A)/2. \quad (12)$$

The NS anisotropy $\xi_z^{\text{GEO}(T)}$ in space in *toward* sector is calculated in every month from ΔGG , as

$$\xi_z^{\text{GEO}(T)} = \Delta GG / (2c_{1,N2}^0 - c_{1,S2}^0 - c_{1,E2}^0) \quad (13)$$

where $c_{1,XX}^0$ is the coupling coefficient for the directional channel XX given, as

$$c_{1,XX}^0 = \frac{1}{\bar{I}_{XX}} \int_{p_{c,XX}}^{\infty} \int_{\Omega_{XX}} \int_{S_{XX}} Y \cdot G(p) \cdot P_1^0(\cos \theta_{or}) dS d\Omega dp \quad (14)$$

with the rigidity spectrum $G(p)$ in (9). We deduce ξ_z^{GEO} from the difference between GG-components in *toward* and *away* days (ΔGG) in equation (12) because of the assumption that the anisotropy vector, when averaged over one month, is symmetric with respect to the heliospheric current sheet (HCS) and the NS anisotropy lies in an opposite direction with the same magnitude above and below the HCS, as

$$\xi_z^{\text{GEO}(A)} = -\xi_z^{\text{GEO}(T)}. \quad (15)$$

2.4. Derivation of modulation parameters

2.4.1. Anisotropy components in the solar wind frame

Three components ($\xi_x^{\text{GEO}(T/A)}$, $\xi_y^{\text{GEO}(T/A)}$, $\xi_z^{\text{GEO}(T/A)}$) of the space anisotropy vector obtained above are first converted to components ($\xi_x^{(T/A)}$, $\xi_y^{(T/A)}$, $\xi_z^{(T/A)}$) in the Geocentric Solar Ecliptic coordinate system (GSE) and then transformed to the solar wind frame for deriving the modulation parameters. We obtain the anisotropy components (ξ_x^{SW} , ξ_y^{SW} , ξ_z^{SW}) in the solar wind frame by subtracting the contribution from the solar wind convection, as

$$\xi_x^{\text{SW}(T/A)} = \xi_x^{(T/A)} - (2 + \Gamma)V_{\text{SW}}^{(T/A)}/c \quad (16a)$$

$$\xi_y^{\text{SW}(T/A)} = \xi_y^{(T/A)} \quad (16b)$$

$$\xi_z^{\text{SW}(T/A)} = \xi_z^{(T/A)} \quad (16c)$$

where $V_{\text{SW}}^{(T/A)}$ is the radial component of the solar wind velocity in the omnitape data (King 2005). We then calculate parallel and perpendicular components of the anisotropy, as

$$\xi_{\parallel}^{(T/A)} = \xi_x^{\text{SW}(T/A)}b_x^{(T/A)} + \xi_y^{\text{SW}(T/A)}b_y^{(T/A)} \quad (17a)$$

$$\xi_{\perp}^{(T/A)} = -\xi_x^{\text{SW}(T/A)}b_y^{(T/A)} + \xi_y^{\text{SW}(T/A)}b_x^{(T/A)} \quad (17b)$$

where $b_x^{(T/A)}$ and $b_y^{(T/A)}$ are GSE components of a unit vector pointing away from the Sun along the IMF and calculated from the mean IMF in the omnitape data. Note that positive $\xi_{\parallel}^{(T/A)}$ and $\xi_{\perp}^{(T/A)}$ correspond to the GCR streaming inward to the inner heliosphere parallel and perpendicular to IMF, respectively. We finally obtain monthly average components of the anisotropy in the solar wind frame, as

$$\xi_{\parallel} = (\xi_{\parallel}^{(T)} + \xi_{\parallel}^{(A)})/2 \quad (18a)$$

$$\xi_{\perp} = (\xi_{\perp}^{(T)} + \xi_{\perp}^{(A)})/2 \quad (18b)$$

$$\xi_z = (\xi_z^{(T)} - \xi_z^{(A)})/2. \quad (18c)$$

This definition of ξ_z is again from the assumption of the symmetry above and below the HCS. Note that the positive ξ_z corresponds to the southward GCR streaming perpendicular to the ecliptic plane in the *toward* IMF sector. We perform calculations of ξ_{\parallel} , ξ_{\perp} , ξ_z described above in every month and deduce the yearly mean value and its error of each anisotropy component from the mean and dispersion of 12 monthly values, respectively. Figure 4 shows ξ_{\parallel} , ξ_{\perp} , ξ_z each as a function of year. It is seen that three components of the anisotropy derived from MD data (solid circles) are all positive throughout the entire period in this figure. A clear 22-year variation seen in ξ_{\parallel} in figure 4a indicates that this component anisotropy is responsible for the phase variation in figure 3 as discovered in Paper I and Paper II. No such clear signature of 22-year variation is seen in either ξ_{\perp} or ξ_z displayed in figures 4b and 4c.

There is a close correlation between the variation of the ξ_{\parallel} values obtained for NMs at 17 GV and for MD at 60 GV (open and solid circles in figure 4a, respectively), indicating a weak rigidity dependence of this anisotropy component. A scatter plot of ξ_{\parallel} for NMs and that for MD on the x and y axes, respectively, yields a correlation coefficient $r=0.92$ and a slope (ratio) of $y/x = \beta = 0.89 \pm 0.05$, which suggests that ξ_{\parallel} remains nearly constant despite the factor of 3.5 difference between the rigidity ranges monitored by NM and MD. On the other hand, we find $\beta = 0.77 \pm 0.07$ for $A > 0$ which is significantly smaller than the value of $\beta = 0.94 \pm 0.005$ found for the $A < 0$ epochs, showing that the rigidity spectrum of ξ_{\parallel} is softer in the $A > 0$ epochs. We also see a remarkable correlation between ξ_{\perp} for NMs and that for MD with $r = 0.75$, while the β values turn out to be 1.65 ± 0.35 (1.26 ± 0.14) in $A > 0$ ($A < 0$) epochs, which indicates that ξ_{\perp} increases with increasing P_m . The most significant difference between NM and MD data is seen in the magnitude of ξ_z shown in figure 4c. For this component, we obtain $\beta = 4.45 \pm 0.61$ (6.08 ± 0.96) for the $A > 0$ ($A < 0$) epochs, which implies that ξ_z increases with increasing rigidity. The correlation between NM and MD data is, however, quite poor ($r = 0.20$) for this component. These features

appearing in figure 4 are qualitatively consistent with ξ_{\perp} and ξ_z increasing with rigidity. The ratios β for the three anisotropy components are listed in the column of “ $P_u=100$ GV” in Table 3 in Appendix B.

We cannot derive any quantitative conclusions about the rigidity spectrum of the anisotropy from the present analysis which assumes a priori a flat spectrum with the upper limiting rigidity P_u fixed at 100 GV as denoted in equation (9). Each value of ratios (β s) described above, for instance, changes for different value of P_u . The rigidity dependences of ξ_{\parallel} , ξ_{\perp} and ξ_z relative to each other, however, remain unchanged even for different value of P_u (see Appendix B). We will discuss the physical origin of these rigidity dependences in the next subsection.

2.4.2. Modulation parameters

Three components (ξ_{\parallel} , ξ_{\perp} , ξ_z) of the anisotropy vector in the solar wind frame obtained above are related to the modulation parameters, i.e. the spatial gradients of GCR density and mean free paths of the pitch angle scattering of GCRs in the turbulent magnetic field, as

$$\xi_{\parallel} = \lambda_{\parallel} G_r \cos \psi \tag{19a}$$

$$\xi_{\perp} = \lambda_{\perp} G_r \sin \psi - R_L G_z \tag{19b}$$

$$\xi_z = R_L G_r \sin \psi + \lambda_{\perp} G_z \tag{19c}$$

where λ_{\parallel} and λ_{\perp} are mean free paths of the pitch angle scattering parallel and perpendicular to the IMF, respectively, R_L is the Larmor radius of GCRs in the IMF and ψ is the IMF spiral angle between the radial direction and a unit vector \mathbf{b} in (17a) and (17b) pointing away from the Sun along the IMF. G_r and G_z are the radial and latitudinal components of

the fractional density gradient vector defined, as

$$\mathbf{G} = \nabla U/U \quad (20)$$

where U is the GCR density (or omnidirectional intensity) given as a function of the position in the heliosphere, time and GCR rigidity. We assume that the longitudinal gradient is zero in our analyses based on the anisotropy averaged over one month which is longer than the solar rotation period. Note that G_z represents the latitudinal density gradient in *toward* sector, being positive when U increases with increasing latitude, and changes its sign in *away* sector due to the assumed symmetry above and below the HCS. The bidirectional latitudinal density gradient $G_{|z|}$, which is defined to be positive (negative) when U increases away from (toward) the HCS, is given by G_z , as

$$G_{|z|} = -\text{sgn}(A)G_z \quad (21)$$

where A represents the polarity of the solar dipole magnetic moment and

$$\begin{aligned} \text{sgn}(A) &= +1, \text{ for } A > 0 \text{ epoch,} \\ &= -1, \text{ for } A < 0 \text{ epoch.} \end{aligned}$$

Equations (19a)-(19c) include four unknown modulation parameters, λ_{\parallel} , λ_{\perp} , G_r and G_z , while we have only three components (ξ_{\parallel} , ξ_{\perp} , ξ_z) of the observed anisotropy. We therefore assume in this paper

$$\lambda_{\perp}/\lambda_{\parallel} = \alpha = 0.01 \quad (22)$$

and derive three remaining parameters, λ_{\parallel} , G_r and G_z . Papers I and II also adopted the same constant value of α based on empirical determinations of $\lambda_{\parallel} \approx 0.5AU$ by Bieber & Pomerantz (1983) and $\lambda_{\perp} \approx 0.007AU$ by Palmer (1982) for ~ 10 GV GCRs. From (19a), we get

$$G_r = \xi_{\parallel} / (\lambda_{\parallel} \cos \psi). \quad (23)$$

Introducing this into (19b), we get

$$G_z = (\alpha\xi_{\parallel} \tan \psi - \xi_{\perp}) / R_L. \quad (24)$$

From (19a), on the other hand, we also get

$$\lambda_{\parallel} = \xi_{\parallel} / (G_r \cos \psi). \quad (25)$$

Introducing (24) and (25) into (19c), we get a quadratic equation for G_r , as

$$R_L \sin \psi G_r^2 - \xi_z G_r - \alpha\xi_{\parallel} (\xi_{\perp} - \alpha\xi_{\parallel} \tan \psi) / (R_L \cos \psi) = 0 \quad (26)$$

which has a solution for positive G_r , as

$$G_r = \left\{ \xi_z + \sqrt{\xi_z^2 + 4\alpha\xi_{\parallel} \tan \psi (\xi_{\perp} - \alpha\xi_{\parallel} \tan \psi)} \right\} / (2R_L \sin \psi). \quad (27)$$

We first calculate $G_{|z|}$ and G_r from equations (24) and (27), respectively, for every month. We then deduce the yearly mean and its error of each parameter from the mean and dispersion of 12 monthly values, respectively. We do not use equation (25) for calculating monthly value of λ_{\parallel} , because G_r , particularly derived from NM data, becomes close to zero in some months resulting in an extremely large λ_{\parallel} and large error of yearly mean λ_{\parallel} . We instead derive yearly mean λ_{\parallel} from yearly mean G_r and $\cos \psi$ in equation (25) and deduce the error by propagating from errors of yearly mean G_r and $\cos \psi$. For R_L for MD and NM data, we use gyro-radii of 60 GV and 17 GV GCRs, respectively, in the monthly mean IMF with the magnitude calculated from the omnitape data.

Figure 5 shows the temporal variations of the calculated modulation parameters, $G_{|z|}$, G_r and λ_{\parallel} . Clearly seen in figure 5a is that the bidirectional latitudinal density gradient ($G_{|z|}$) is positive (indicating the local minimum of density on the HCS) in $A > 0$ epoch, while it is negative (indicating the local maximum of density on the HCS) in $A < 0$ epoch, in accord with the drift model prediction (Kóta & Jokipii 1983). There is no clear signature

of an 11-year variation in $G_{|z|}$. The 22-year variation of $G_{|z|}$ appears cleaner and statistically more significant with relatively smaller errors in MD data than in NM data. The mean $G_{|z|}$ derived from MD (NM) data is 0.42 ± 0.05 (0.86 ± 0.14) %/AU in $A > 0$, while it is -0.52 ± 0.04 (-1.47 ± 0.15) %/AU, indicating that the magnitude of $G_{|z|}$ is larger in $A < 0$ than in $A > 0$ in both MD and NM data.

The radial density gradient (G_r) in figure 5b, on the other hand, varies with ~ 11 -year solar activity cycle with maxima (minima) in solar maximum (minimum) periods (Papers I and II; Bieber & Pomerantz 1986), but there is no significant difference seen between mean G_r s in $A > 0$ and $A < 0$ epochs. The mean G_r deduced from MD (NM) data is 0.89 ± 0.11 (1.04 ± 0.08) %/AU in $A > 0$ epoch, while it is 0.99 ± 0.12 (1.13 ± 0.10) %/AU in $A < 0$ epoch. It is noted that we find a poor correlation between temporal variations of $G_{|z|}$ and G_r in both NM and muon data.

The parallel mean free path ($\lambda_{||}$) in figure 5c also changes with the solar activity cycle with minima (maxima) in solar maximum (minimum) periods. The mean $\lambda_{||}$ deduced from MD (NM) data is 0.90 ± 0.10 (0.89 ± 0.06) AU in $A > 0$, while it is 1.32 ± 0.13 (1.14 ± 0.10) AU in $A < 0$. This indicates that the mean $\lambda_{||}$ is systematically larger in $A < 0$ than in $A > 0$ at 2 or 3 sigma level. It is also interesting that $\lambda_{||}$ s in NM and MD data appear like persistently increasing toward maxima in 2008 and 2009 during the last three solar activity cycles, while G_r s look like decreasing. The parallel mean free path ($\lambda_{||}$) deduced from NM data (open circles) shows peaks in 1985 and 2008 in $A < 0$ solar minimum epochs, while it shows smaller peaks in 1974 and 1997 in $A > 0$ solar minimum epochs. This is qualitatively consistent with results reported in Paper I. In $\lambda_{||}$ deduced from MD data (solid circles), on the other hand, the 11-year variation is more prominent with maxima in every solar minimum in 1976, 1987, 1997 and 2009, but no clear 22-year variation is visible in this figure. We will discuss long-term variations of G_r and $\lambda_{||}$ in more detail in the next section.

We now discuss the rigidity dependence of each modulation parameter. Figure 6 shows the correlation between the parameters derived from NM data at 17 GV and from MD data at 60 GV. In $A > 0$ ($A < 0$) epoch, $G_{|z|}$ from NM and MD data in the left panel shows a good correlation with r of 0.63 (0.86), while the mean ratio ($\beta = y/x$) of $G_{|z|}$ from MD data to that from NM data is 0.48 ± 0.10 (0.35 ± 0.05) in $A > 0$ ($A < 0$) epoch indicating that $G_{|z|}$ decreases with increasing P_m . Also similar but weaker correlations are seen in G_r and λ_{\parallel} in the middle and right panels with the average r of 0.53 (0.58) and 0.21 (0.54), respectively, while the mean β s of G_r and λ_{\parallel} are 0.85 ± 0.12 (0.87 ± 0.13) and 1.00 ± 0.13 (1.16 ± 0.15), respectively, indicating that these parameters are almost independent of P_m . Note that β of $G_{|z|}$ is significantly smaller than β of G_r indicating the softer rigidity dependence of $G_{|z|}$ than that of G_r , when P_u is fixed at 100 GV. The ratio β s derived from different P_u are listed in Table 3 in Appendix B.

We finally discuss the physical origin of the rigidity dependence of each anisotropy component presented in the preceding subsection. As expressed in equations (19a)-(19c), ξ_{\perp} and ξ_z include contributions from the drift (i.e. the diamagnetic drift) added to the perpendicular diffusion, while ξ_{\parallel} results solely from the parallel diffusion. By using G_r , $G_{|z|}$ and λ_{\parallel} with an assumption of $\lambda_{\perp} = \alpha \lambda_{\parallel} = 0.01 \lambda_{\parallel}$, we calculate individual contributions from the diffusion and drift to each of ξ_{\perp} and ξ_z . We find that the mean diffusion contribution ($\lambda_{\perp} G_r \sin \psi$) to ξ_{\perp} is significantly smaller than the mean drift contribution ($-R_L G_z$) in both NM and MD data, hence ξ_{\perp} is mainly arising from the drift effect. The mean ratio of $|\lambda_{\perp} G_r \sin \psi|$ to $|-R_L G_z|$ contributing to ξ_{\perp} is 0.08 ± 0.02 in NM data, while the ratio is 0.07 ± 0.02 in MD data indicating that the mean contribution from the diffusion to ξ_{\perp} is less than 10 % in both NM and MD data independent of P_m . The mean ratio of the diffusion ($|\lambda_{\perp} G_z|$) to the drift ($|R_L G_r \sin \psi|$) contributing to ξ_z is also small as 0.03 ± 0.01 in MD data. The ratio in NM data, on the other hand, is 0.19 ± 0.03 and significantly larger than the ratio in MD data, indicating that the relative contribution of the diffusion to ξ_z

increases with decreasing P_m . This is due to the rigidity dependence of $G_{|z|}$, which is softer than that of G_r as discussed above. Since there is only a poor correlation between temporal variations of $G_{|z|}$ and G_r in figure 5, this may explain the poor correlation between ξ_z s by NM and MD data which is shown in the bottom panel of figure 4 and discussed in the preceding subsection.

3. Summary and Discussions

We examined the energy dependence of the long-term variations of the 3D anisotropy of GCR intensity by analyzing the data recorded in 1970-2013 by NMs (Swarthmore/Newark, Alert/Thule and McMurdo) which have median responses to ~ 17 GV primary GCRs and the Nagoya MD which has the median response to ~ 60 GV GCRs. The derived free-space harmonic vector of the diurnal anisotropy changes its phase to earlier hours in $A > 0$ solar minima from the $\sim 18:00$ local time known as the phase of the “corotation” anisotropy, while the amplitude changes in 11-year cycle decreasing to a small value in years around every solar minimum. We note that the magnitude of the phase change is significantly larger in MD data than in NM data indicating a marked rigidity dependence of the phase change. A clear 22-year variation is seen in the parallel component (ξ_{\parallel}) of the anisotropy confirming the conclusion of Paper II that ξ_{\parallel} is primarily responsible for the phase change. The north-south anisotropy (ξ_z) derived from the GG-component of Nagoya MD also shows an 11-year cycle with minima in years around every solar minimum.

The ecliptic anisotropy components (ξ_{\parallel} and ξ_{\perp}) derived from NM and MD data vary in a close correlation with each other, while no such correlation is seen in the variation of ξ_z . The mean ratio between ξ_{\parallel} s in MD and that in NM data is roughly consistent with a rigidity independent spectrum, while the rigidity spectrum of ξ_{\parallel} is systematically softer in $A > 0$ than in $A < 0$. On the other hand, ξ_{\perp} and ξ_z derived from MD data are

significantly larger than those from NM data, indicating that these components increase with P_m . According to equations (19a)-(19c), ξ_{\perp} and ξ_z include contributions from the gyration of particles (connected to diamagnetic drift) added to perpendicular diffusion, while ξ_{\parallel} is caused by the parallel diffusion alone. It is reasonable, therefore, to expect that the observed harder rigidity spectra of ξ_{\perp} and ξ_z are due to effects from drift. Based on numerical simulations of particle propagation in turbulent magnetic field, Minnie et al. (2007) has shown that drifts are suppressed by magnetic turbulence, but the suppression sets in at lower turbulence amplitudes for low-energy than for high-energy cosmic rays. This may give a possible explanation for why the contribution of drift streaming results in a harder rigidity spectrum. If this is the case, we may well need two different spectra, representing diffusion and drift, combined in ξ_{\perp} and ξ_z , to reproduce the correct rigidity dependence of the diurnal anisotropy in space. We will present such analyses elsewhere.

Equations (19a)-(19c) also imply that the drift contribution to ξ_{\perp} is proportional to $G_{|z|}$, while the drift contribution to ξ_z is proportional to G_r . By comparing G_r and $G_{|z|}$ derived from NM and MD data, we find that the rigidity dependences of G_r and ξ_z are harder than those of $G_{|z|}$ and ξ_{\perp} . Yasue (1980) and Hall et al. (1994) analyzed the north-south anisotropy observed with NMs and MDs monitoring a wide range of P_m and found ξ_z increasing with the rigidity up to several hundred GV. This is in a qualitative agreement with the present paper.

We finally discuss the long-term variations of the modulation parameters. Figure 7 shows the temporal variation of $\lambda_{\parallel}G_r = \xi_{\parallel}/\cos\psi$ (see equation (19a)). Clearly seen is that the mean magnitude of $\lambda_{\parallel}G_r$ is significantly smaller in $A > 0$ (solid circles) than in $A < 0$ periods (open circles). The mean magnitude of $\lambda_{\parallel}G_r$ derived from MD data and that from NM data in $A < 0$ epoch are 1.07 ± 0.03 and 1.14 ± 0.02 , respectively, which are fairly consistent with each other. The mean magnitudes in $A > 0$ periods are 0.68 ± 0.04 %

and 0.89 ± 0.05 %, respectively. Combined with the solar wind convection, this reduction of $\lambda_{\parallel} G_r$ results in the observed phase shift of the diurnal anisotropy to earlier hours in $A > 0$ as suggested by Paper I. We also note that the ratio of $\lambda_{\parallel} G_r$ for MD to that for NM data is smaller in $A > 0$ than in $A < 0$ periods, indicating the softer rigidity spectrum of this component for $A > 0$ than for $A < 0$ (see discussion of figure 4 in the preceding section). This larger decrease of $\lambda_{\parallel} G_r$ in $A > 0$ epoch in MD data than in NM data is responsible to the larger phase shift of the diurnal anisotropy in $A > 0$ solar minimum epoch in MD data. The harder rigidity spectrum of ξ_{\perp} than that of ξ_{\parallel} mentioned above is also partly responsible to the larger phase shift in MD data in $A > 0$ minimum epochs. Hall et al. (1997) used the NM and MD data for analyzing the rigidity spectrum of the diurnal anisotropy and obtained the average $G(p)$ proportional to $p^{-0.1 \pm 0.2}$ with $P_u = 100 \pm 25$ GV. Although their spectrum seems to be consistent with $G(p)$ assumed in this paper, such a common spectrum for ξ_{\parallel} and ξ_{\perp} cannot reproduce the observed feature that the phase shift observed by MD in $A > 0$ solar minimum epoch is significantly larger than that by NM.

The 11- and 22-year variations are also apparent in the modulation parameters shown in figure 5. The bidirectional latitudinal density gradient ($G_{|z|}$) in the top panel is positive (negative) in $A > 0$ ($A < 0$) epoch in accord with the drift model prediction of the local minimum (maximum) of GCR density around the HCS. This 22-year variation looks more significant in MD data than in NM data, with a smaller error of each data point. The mean magnitude of $G_{|z|}$ is larger in $A < 0$ than in $A > 0$ in both MD and NM data. The 11-year variation is evident in the radial density gradient (G_r) in the middle panel of figure 5, while we cannot identify a clear 22-year variation as reported by Bieber & Pomerantz (1986). The mean G_r deduced from MD (NM) data is 0.89 ± 0.11 (1.04 ± 0.08) %/AU in $A > 0$ epoch, while it is 0.99 ± 0.12 (1.13 ± 0.10) %/AU in $A < 0$ epoch. It is noted that we find a poor correlation between temporal variations of $G_{|z|}$ and G_r in both NM and muon data.

The mean parallel mean free path (λ_{\parallel}), on the other hand, turns out to be significantly larger in the $A < 0$ than in the $A > 0$ epochs, in the both MD and NM data. We find that the mean λ_{\parallel} deduced from MD (NM) data is 0.90 ± 0.10 (0.89 ± 0.06) AU in $A > 0$, while it is 1.32 ± 0.13 (1.14 ± 0.10) AU in $A < 0$. Paper I suggested that the 22-year variation of λ_{\parallel} is responsible for the reduction of $\lambda_{\parallel} G_r$ in $A > 0$ and for the 22-year variation of the diurnal anisotropy. The two bottom panels of figure 7 show the correlation between G_r and λ_{\parallel} (both in logarithmic scale) on the vertical (y) and horizontal (x) axes, respectively. Since λ_{\parallel} on the x -axis is deduced from $\lambda_{\parallel} G_r$ divided by G_r on the y -axis, data points in this scatter plot align on a straight line when $\lambda_{\parallel} G_r$ is constant during the analysis period. Solid and dashed straight lines in each panel display functions of $y = c/x$ best-fitting to data in $A > 0$ and $A < 0$ epochs, respectively, each with the intercept c as a best-fit parameter. It is seen that, for the MD data (left panel) the best-fit c for $A > 0$ data (solid circles) is about 64 % of that for the $A < 0$ data (open circles). This is consistent with the lower λ_{\parallel} value derived from MD data for $A > 0$ epochs which is 68 % ($=0.90/1.32$) of that in $A < 0$ epoch, indicating that the 22-year variation of $\lambda_{\parallel} G_r$ in the left panel is due to the 22-year variation of λ_{\parallel} on the horizontal axis.

However, as mentioned in connection with figure 5 in the preceding section, we also find that $\lambda_{\parallel s}$ ($G_r s$) from NM and MD data appear to persistently increase (decrease) during the last three solar activity cycles reaching maximum (minimum) in 2008-2009. Figure 8 displays the mean G_r and λ_{\parallel} in $A > 0$ and $A < 0$ epochs, each as a functions of time. It is clear particularly in the MD data (left panels) that there is a long-term trends indicated by a best-fit solid line in each panel. This trend enhances the difference between $A > 0$ and $A < 0$ means of λ_{\parallel} , while it reduces the difference between means of G_r . The simple means of G_r or λ_{\parallel} in all $A > 0$ and $A < 0$ epochs are, therefore, seriously biased by these long term trends. If we look at the deviation of each data point from the solid line in the MD data, on the other hand, we find that G_r and λ_{\parallel} are both larger (smaller) in $A < 0$ ($A > 0$)

epoch, although only at one sigma level.

The phase-shift of the diurnal anisotropy toward earlier hours in the $A > 0$ epochs is a robust consequence of particle drifts in the inhomogeneous large-scale HMF (heliospheric magnetic fields). The observed phase shift in $A > 0$ epoch arises naturally in various drift models employing different approaches (Levy 1976; Erdös & Kóta 1980; Potgieter & Moraal 1985). The reproduction of the north-south anisotropy, which is formed by the interplay of drift and perpendicular diffusion, is more challenging for theoretical models. This is particularly true for the $A > 0$ epoch, when latitudinal gradients tend to point away from the current sheet, but the intensity minimum of GCRs is not precisely on the HCS. Hence one cannot expect a one-to-one correlation between the field polarity and the NS anisotropy (Okazaki et al. 2008). Kóta & Jokipii (2001) modeled the 3D anisotropy in a simulation including a wavy HCS with possible variations in the solar wind speed leading to the formation of corotating interaction regions. Their results are in qualitative agreement with the observed phase-shift and reduction of radial gradient in the $A > 0$ epochs as well as with the opposite sense of latitudinal gradient around the HCS around solar minima of $A > 0$ and $A < 0$ epochs. The simulation results for the variation of the NS anisotropy remained inconclusive.

It is important to keep in mind that solar cycles are not identical and, as mentioned in the previous section, long-term changes do occur. A particularly interesting recent example is the long and unusual last solar cycle, when the GCR intensity at the Earth reached record-high level (Mewaldt et al. 2010). The most plausible explanation is that the magnetic field was weakest ever recorded (McComas et al. 2008) and the weaker field allowed faster diffusion of GCRs into the inner part of the heliosphere. Another remarkable feature of the last solar cycle was that the HCS remained tilted for a long time and did not flatten the same way as in other cycles. Figure 4 shows that ξ_z turned out to be larger

in the last solar minimum than during previous solar minima. This most likely shows the effect of the tilted HCS. The streaming component normal to the HCS cannot abruptly change, but has to change continuously at the HCS. Hence ξ_z has to go to a small value when the HCS flattens, while it can be larger if the HCS is tilted. This feature is more apparent for MD data than for NM data.

The dynamic range of λ_{\parallel} (or G_r) due to the 11-year variation in the lower panels of figure 7 is close to an order of magnitude and much larger than the 22-year variation. Small signature of its 22-year variation can be easily masked by the 11-year variation with much larger amplitude. In order to analyze the 22-year variation of each modulation parameter, therefore, it is necessary to minimize the influence of the 11-year variation as much as possible. Also simple means of λ_{\parallel} and G_r in each of $A > 0$ and $A < 0$ epochs may be seriously biased by their long term trends as seen above. For identifying the physical origin of the 22-year variation correctly, it is also necessary to analyze its rigidity dependence. The long-term observation with the Nagoya MD, as well as the observations with NMs, makes such analyses possible.

This work is supported in part by the joint research program of the Solar-Terrestrial Environment Laboratory (STEL), Nagoya University. The observations with the Nagoya multi-directional muon detector are supported by the Nagoya University. The Bartol Research Institute neutron monitor program, which operates Newark, Thule and McMurdo neutron monitors, is supported by National Science Foundation grant ATM-0000315. We thank the World Data Center for Cosmic Rays, Solar-Terrestrial Environment Laboratory, Nagoya University, for providing the neutron monitor data analyzed in this paper. Wilcox Solar Observatory data used in this study was obtained via the web site <http://wso.stanford.edu> at 2014:03:19_01:10:41 PDT courtesy of J.T. Hoeksema. The Wilcox Solar Observatory is currently supported by NASA. JK thanks for the support and

hospitality of the STEL and the Shinshu University supplied during his stay as the visiting professor of the STEL.

A. Appendix: Numerical data of anisotropy components and modulation parameters obtained in the present paper

For readers references, we list in Table 2 numerical data of the anisotropy and modulation parameters derived from MD data at 60 GV. Note that the amplitude and phase in these tables are corrected for the Compton-Getting effect arising from the Earth’s orbital motion around the Sun (see section 2.2 in the text). We confirmed that the anisotropy components derived from NMs by us in each year are fairly consistent with the components given in Paper I (see Table 2 in their paper), which analyzed the same NM data in the similar manner during an overlapping period between 1970 and 1988. The amplitude and phase of the common vector derived in our analyses of the MD data are shown in figure 9 (see text). It is seen that the amplitude of the common vector is small and the phase is almost stable around $\sim 06:00$ local solar time.

B. Appendix: Dependence on the upper limiting rigidity

Following analyses in Papers I and II, we assumed in this paper the rigidity spectrum of the anisotropy in equation (9) with γ and P_u fixed at 0 and 100 GV respectively. This choice of the spectrum is rather subjective, lacking firm physical or observational proof. In this section, we show how β (the ratio between anisotropies and modulation parameters derived from NM and MD data) depends on the upper limiting rigidity (P_u) assumed and that our major conclusions on the rigidity dependence derived from β are not affected by changing P_u . Figure 10 displays anisotropy components derived from MD data with three different P_u s. We choose this range of P_u between 100 and 300 GV referring to the solar cycle variation of P_u reported in Munakata et al. (1997). We confirmed that the anisotropy derived from NM data is almost insensitive to changing P_u as pointed by Paper II, while the anisotropy derived from MD data changes significantly. The increase of P_u with the same spectral index (γ) results in the reduction of the amplitude of the free space anisotropy. It also results in the phase of the diurnal anisotropy in free space shifting to earlier hours, due to the reduced average deflection of GCR orbits in the geomagnetic field. Features of anisotropy components in figure 10 changing with P_u are interpreted in terms of these natures of the free space anisotropy. Table 3 lists mean β for three P_u s. Firstly, the mean $\beta_{\xi_{\parallel}}$ close to (or slightly smaller than) one for all P_u s indicate ξ_{\parallel} being similar in NM and MD data, while it is significantly smaller in $A > 0$ than in $A < 0$ for each P_u . Second, the mean $\beta_{\xi_{\perp}}$ and β_{ξ_z} are both significantly larger than one indicating harder rigidity spectra of ξ_{\perp} and ξ_z than that of ξ_{\parallel} . The mean β_{ξ_z} is always larger than the mean $\beta_{\xi_{\perp}}$. Third, the mean $\beta_{G_{|z|}}$ and β_{G_r} are significantly smaller than one for all P_u s.

REFERENCES

- Agrawal, S. P. 1983, *Space Sci. Rev.*, 34, 127
- Ahluwalia, H. S. 1988, *Geophys. Res. Lett.*, 15, 287
- Amenomori, M. ET AL. 2004, *Phys. Rev. Lett.*, 93, 061101
- Bieber, J. W., & Pomerantz, M. A. 1983, *Geophys. Res. Lett.*, 10, 920
- Bieber, J. W., & Pomerantz, M. A. 1986, *ApJ*, 303, 843
- Bieber, J. W., Evenson, P. & Matthaeus, W. 1987, *Geophys. Res. Lett.*, 14, 864
- Bieber, J. W., & Chen, J. 1991, *ApJ*, 372, 301 (Paper II)
- Cane, H. V., Richardson, I. G., & von Roseninge, T. T. 1996, *J. Geophys. Res.*, 101, 21561
- Chapman, S., & Bartels, J. 1940, *Geomagnetism*, 2, 611, Oxford University Press, Oxford
- Chen, J., & Bieber, J. W. 1993, *ApJ*, 405, 375 (Paper I)
- Compton, A. H., & Getting, I. A. 1935, *Physical Review*, 47, 817
- Cutler, D. J., & Groom, D. E. 1986, *Nature*, 322, 434
- Erdős, G., & Kóta, J. 1980, *Ap&SS*, 67, 45
- Forbush, S. E. 1967, *J. Geophys. Res.*, 72, 4937
- Fujimoto, K., Inoue, A., Murakami, K., & Nagashima, K. 1984, *Coupling Coefficients of Cosmic Ray Daily Variations for Neutron Monitor Stations (CRRL Rep., No. 9; Nagoya, Japan: Cosmic-Ray Research Laboratory)*
- Gleeson, L. J., & Axford, W. I. 1967, *ApJ*, 149, L115

- Gleeson, L. J. 1969, *Planet. Space Sci.*, 17, 31
- Hall, D. L., Humble, J. E., & Duldig, M. L. 1994, *J. Geophys. Res.*, 99, 21433
- Hall, D. L., Duldig, M. L., & Humble, J. E. 1996, *Space Sci. Rev.*, 78, 449
- Hall, D. L., Duldig, M. L., & Humble, J. E. 1997, *ApJ*, 482, 1038
- Jokipii, J. R., & Kopriva, D. A. 1979, *ApJ*, 234, 384
- Jokipii, J. R., & Kóta, J. 1982, *Geophys. Res. Lett.*, 9, 656
- Jordan, A. P., Spence, H. E., Blake, J. B., & Shaul, D. N. A. 2011, *J. Geophys. Res.*, 9, 656
- King, J. H., & N.E. Papitashvili 2005, *J. Geophys. Res.*, 110, A02104
- Kóta, J., & Jokipii, J. R. 1983, *ApJ*, 265, 573
- Kóta, J., & Jokipii, J. R. 2001, *Adv. Space Res.*, 27, 607
- Laurenza, M., & Storini, M. 2003, *J. Geophys. Res.*, 108, 1069
- Levy, E. H. 1976, *J. Geophys. Res.*, 81, 2082
- Lin, Z., Bieber, J. W., & Evenson, P. 1995, *J. Geophys. Res.*, 100, 23543
- McComas, D. J., Ebert, R. W., Elliott, H. A., Goldstein, B. E., Gosling, J. T., Schwadron, N. A., Skoug, R. M. 2008, *Geophys. Res. Lett.*, 35, L18103
- Mewaldt, R. A., Davis, A. J., Lave, K. A., Leske, R. A., Stone, E. C., Wiedenbeck, M. E., Binns, W. R., Christian, E. R., Cummings, A. C., de Nolfo, G. A., Israel, M. H., Labrador, A. W., von Rosenvinge, T. T. 2010, *ApJ*, 723, L1
- Minnie, J., Bieber, J. W., Matthaeus, W. H., Burger, R. A. 2007, *ApJ*, 670, 1149
- Mori, S., & Nagashima, K. 1979, *Planet. Space Sci.*, 27, 39

- Munakata, K., Miyasaka, H., Hall, D. L., Yasue, S., Kato, C., Fujii, Z., Fujimoto, K., & Sakakibara, S. 1997, Proc. 25th Internat. Cosmic Ray Conf.(Durban), 2, 77
- Munakata, K., Miyasaka, M., Sakurai, I., Yasue, S., Kato, C., Akahane, S., Koyama, S., Hall, D. L., Fujii, Z., Fujimoto, K., Sakakibara, S., Humble, J. E., & Duldig, M. L. 2002, Adv. Space Res., 29, 1527
- Murakami, K., Nagashima, K., Sagisaka, S., Mishima, Y., & Inoue, A. 1979, Il Nuovo Cim., 2C, 635
- Nagashima, K., Fujimoto, K., Fujii, Z., Ueno, H., & Kondo, I. 1972, Rep. Ionos. Space Res. Jpn., 26, 31
- Nagashima, K., Sakakibara, S., Fenton, A. G., & Humble, J. E. 1985, Planet. Space Sci., 33, 395
- Oh, S. Y., Yi, Y., & Bieber, J. W. 2010, Sol. Phys., 262, 199
- Okazaki, Y., ET AL. 2008, ApJ, 681, 693
- Palmer, I. D. 1982, Rev. Geophys. Space Phys., 20, 335
- Parker, E. N. 1958, ApJ, 128, 664
- Parker, E. N. 1965, Planet. Space Sci., 13, 9
- Potgieter, M. S., & Moraal, H. 1985, ApJ, 294, 425
- Swinson, D. B. 1969, J. Geophys. Res., 74, 5591
- Thambyahpillai, T. & Eliot, H. 1953, Nature, 171, 918
- Yasue, S. 1980, J. Geomag. Geoelectr., 32, 617

Yasue, S., Sakakibara, S., & Nagashima, K. 1982, Coupling Coefficients of Cosmic Ray
Daily Variations for Neutron Monitor Stations (CRRL Rep., No. 7; Nagoya, Japan:
Cosmic-Ray Research Laboratory)

Table 1. Neutron Monitors (NMs) and Muon Detectors (MD) used in this paper

Detector type	Station (geographic lat., long.)	P_c (GV)	P_m (GV)
NM ^a	Swarthmore/Newark (39.70°, -75.70°)	2.0 GV	17.0 GV
	Thule (76.60°, -68.80°)	0.0 GV	17.0 GV
	Alert (82.50°, -62.30°)	0.0 GV	17.0 GV
	McMurdo (-77.95°, 166.60°)	0.0 GV	17.0 GV
	Nagoya (35.15°, 139.97°)		
	Directional channel		
MD	V	10.1 GV	59.4 GV
	N	10.8 GV	64.6 GV
	S	10.0 GV	62.6 GV
	E	12.8 GV	66.7 GV
	W	9.7 GV	61.8 GV
	NE	12.9 GV	72.0 GV
	NW	9.1 GV	66.6 GV
	SE	11.5 GV	69.3 GV
	SW	9.5 GV	65.6 GV
	N2	8.6 GV	83.0 GV
	S2	9.5 GV	80.5 GV
	E2	13.2 GV	88.3 GV
	W2	8.7 GV	79.3 GV
	N3	8.7 GV	105.0 GV
S3	9.5 GV	103.7 GV	
E3	17.1 GV	113.7 GV	
W3	8.6 GV	103.0 GV	

Note. — The geomagnetic cut-off rigidity (P_c) and median primary rigidity (P_m) in GV are listed for each directional channel together with the geographic latitude and longitude of the location of the detector in degrees. The Nagoya MD has 17 directional channels, while each NM measures only omni-directional intensity which is regarded as the vertical intensity on average.

^aFor deriving the diurnal anisotropy at 17 GV, we use Swarthmore NM data for a period between 1970 and 1978, while we use Newark NM data for a period between 1979 and 2013. For deriving the north-south anisotropy at 17 GV, we use Thule and McMurdo NMs for two periods, one between 1970 and 1975 and the other between 1979 and 2013, while we use Alert and McMurdo for a period between 1976 and 1978.

Table 2. Anisotropy components and modulation parameters derived from the Nagoya MD data

year	sgn(A) ^a	Amplitude [%]	Phase [hour]	ξ_{\parallel} [%]	ξ_{\perp} [%]	ξ_z [%]	$G_{ z }$ [%/AU]	G_r [%/AU]	λ_{\parallel} [AU]
1970	*	0.39±0.07	17.1±0.4	0.63±0.01	0.15±0.01	0.33± 0.02	*	1.03±0.05	1.02±0.14
1971	*	0.42±0.04	15.9±0.3	0.60±0.04	0.08±0.03	0.26± 0.04	*	1.03±0.21	0.89±0.19
1972	+	0.34±0.02	15.9±0.3	0.49±0.03	0.12±0.04	0.26± 0.03	0.32±0.09	1.00±0.09	0.76±0.08
1973	+	0.41±0.03	15.3±0.3	0.55±0.04	0.06±0.03	0.27± 0.05	0.17±0.08	1.28±0.22	0.57±0.11
1974	+	0.42±0.03	16.3±0.3	0.70±0.04	0.13±0.03	0.32± 0.05	0.43±0.09	1.58±0.23	0.61±0.10
1975	+	0.34±0.03	14.6±0.3	0.45±0.02	0.11±0.05	0.20± 0.03	0.27±0.15	0.71±0.08	0.86±0.11
1976	+	0.21±0.03	13.9±0.5	0.42±0.04	0.24±0.02	0.12± 0.02	0.61±0.05	0.52±0.06	1.10±0.15
1977	+	0.24±0.04	14.5±0.5	0.38±0.03	0.22±0.05	0.22± 0.04	0.59±0.13	0.86±0.15	0.67±0.13
1978	+	0.44±0.04	15.5±0.4	0.50±0.04	0.06±0.04	0.28± 0.06	0.20±0.13	1.30±0.28	0.62±0.14
1979	*	0.48±0.03	16.3±0.2	0.61±0.03	0.02±0.03	0.27± 0.04	*	1.38±0.22	0.68±0.12
1980	*	0.43±0.03	17.3±0.4	0.64±0.03	0.13±0.04	0.23± 0.03	*	0.99±0.11	1.06±0.12
1981	−	0.47±0.03	17.4±0.2	0.73±0.04	0.12±0.03	0.27± 0.03	-0.44±0.10	1.38±0.17	0.80±0.10
1982	−	0.45±0.05	17.5±0.3	0.76±0.06	0.13±0.04	0.29± 0.05	-0.50±0.15	2.01±0.33	0.54±0.10
1983	−	0.47±0.05	17.9±0.4	0.84±0.05	0.17±0.03	0.28± 0.05	-0.60±0.11	1.72±0.22	0.69±0.10
1984	−	0.56±0.04	18.0±0.2	0.92±0.04	0.07±0.02	0.28± 0.04	-0.27±0.07	1.92±0.20	0.64±0.08
1985	−	0.48±0.04	18.1±0.3	0.82±0.04	0.13±0.05	0.18± 0.03	-0.36±0.13	0.85±0.11	1.35±0.17
1986	−	0.25±0.04	16.8±0.5	0.58±0.04	0.20±0.04	0.10± 0.02	-0.50±0.11	0.50±0.07	1.62±0.24
1987	−	0.33±0.05	18.3±0.4	0.70±0.06	0.24±0.03	0.05± 0.04	-0.72±0.13	0.46±0.08	2.22±0.39
1988	−	0.40±0.04	18.0±0.3	0.71±0.05	0.24±0.03	0.21± 0.03	-0.82±0.07	0.97±0.13	1.17±0.18

Table 2—Continued

year	sgn(A) ^a	Amplitude [%]	Phase [hour]	ξ_{\parallel} [%]	ξ_{\perp} [%]	ξ_z [%]	$G_{ z }$ [%/AU]	G_r [%/AU]	λ_{\parallel} [AU]
1989	—	0.46±0.04	18.3±0.3	0.81±0.05	0.19±0.05	0.15± 0.04	-0.65±0.18	0.94±0.19	1.23±0.25
1990	*	0.51±0.05	17.9±0.2	0.82±0.04	0.04±0.05	0.28± 0.03	*	1.49±0.14	0.73±0.08
1991	*	0.52±0.05	18.3±0.3	0.87±0.05	0.18±0.04	0.14± 0.05	*	1.02±0.28	1.25±0.35
1992	+	0.45±0.04	15.4±0.4	0.48±0.04	0.06±0.06	0.21± 0.03	0.22±0.22	1.12±0.19	0.67±0.13
1993	+	0.37±0.04	15.2±0.4	0.50±0.04	0.08±0.04	0.18± 0.04	0.25±0.14	0.86±0.14	0.81±0.15
1994	+	0.36±0.03	15.1±0.4	0.57±0.05	0.15±0.03	0.24± 0.05	0.45±0.09	1.20±0.21	0.63±0.12
1995	+	0.24±0.03	14.1±0.4	0.36±0.04	0.23±0.03	0.20± 0.04	0.60±0.08	0.73±0.16	0.77±0.18
1996	+	0.16±0.03	13.6±0.9	0.40±0.05	0.27±0.04	0.10± 0.02	0.61±0.08	0.37±0.07	1.47±0.28
1997	+	0.19±0.02	13.1±0.3	0.28±0.03	0.26±0.02	0.06± 0.03	0.65±0.04	0.25±0.05	1.84±0.35
1998	+	0.32±0.04	15.3±0.5	0.46±0.06	0.16±0.05	0.13± 0.07	0.49±0.15	0.62±0.17	1.16±0.33
1999	*	0.48±0.02	16.4±0.2	0.63±0.03	0.07±0.03	0.15± 0.04	*	0.78±0.15	1.27±0.25
2000	*	0.44±0.03	17.4±0.3	0.72±0.03	0.16±0.03	0.21± 0.06	*	1.01±0.22	1.11±0.24
2001	—	0.45±0.04	16.9±0.4	0.65±0.05	0.12±0.04	0.19± 0.05	-0.33±0.12	0.89±0.22	1.18±0.30
2002	—	0.47±0.05	17.8±0.4	0.77±0.06	0.15±0.04	0.21± 0.04	-0.57±0.13	1.16±0.18	1.02±0.18
2003	—	0.45±0.04	18.2±0.3	0.92±0.03	0.25±0.05	0.23± 0.04	-0.88±0.16	1.36±0.16	0.92±0.11
2004	—	0.46±0.03	17.4±0.3	0.74±0.04	0.14±0.03	0.29± 0.04	-0.41±0.07	1.30±0.16	0.85±0.12
2005	—	0.48±0.04	17.9±0.3	0.83±0.05	0.18±0.03	0.19± 0.02	-0.51±0.09	0.88±0.10	1.35±0.16
2006	—	0.36±0.03	17.5±0.4	0.64±0.05	0.21±0.03	0.22± 0.03	-0.45±0.06	0.69±0.10	1.44±0.22
2007	—	0.33±0.03	17.4±0.2	0.65±0.03	0.22±0.02	0.15± 0.03	-0.43±0.04	0.51±0.06	1.87±0.20

Table 2—Continued

year	sgn(A) ^a	Amplitude [%]	Phase [hour]	ξ_{\parallel} [%]	ξ_{\perp} [%]	ξ_z [%]	$G_{ z }$ [%/AU]	G_r [%/AU]	λ_{\parallel} [AU]
2008	—	0.27±0.02	17.4±0.3	0.64±0.03	0.26±0.02	0.17± 0.02	-0.49±0.04	0.50±0.07	1.85±0.25
2009	—	0.21±0.02	16.8±0.3	0.45±0.02	0.26±0.02	0.12± 0.02	-0.44±0.04	0.28±0.04	2.76±0.39
2010	—	0.34±0.03	17.6±0.3	0.62±0.03	0.21±0.04	0.18± 0.03	-0.43±0.07	0.56±0.08	1.72±0.24
2011	—	0.35±0.03	17.9±0.3	0.67±0.04	0.22±0.03	0.26± 0.03	-0.53±0.08	0.88±0.10	1.17±0.14
2012	*	0.36±0.05	17.5±0.3	0.62±0.05	0.23±0.04	0.26± 0.05	*	0.93±0.17	1.12±0.21
2013	*	0.38±0.04	17.7±0.3	0.65±0.04	0.18±0.04	0.24± 0.04	*	0.76±0.14	1.34±0.25

Note. — The amplitude and phase (the local solar time of maximum intensity) of the space harmonic vector in figure 3, three components (ξ_{\parallel} , ξ_{\perp} , ξ_z) of the anisotropy in the solar wind frame in figure 4 and modulation parameters ($G_{|z|}$, G_r , λ_{\parallel}) in figure 5, all derived from the Nagoya MD data, are listed for each year. Yearly mean value and error are deduced from the average and dispersion of monthly values, respectively.

^aEach character in the column “sgn(A)” indicates the polarity of the large-scale solar magnetic field assigned by us referring to the Solar Polar Field Strength available at the WSO web-site; “+” for a year in $A > 0$ epoch, “−” for a year in $A < 0$ epoch and “*” for a year when the polarity reversal is in progress (see text).

Table 3. Mean β values obtained with three different P_u s in equation (9)

	polarity	$P_u = 100$ GV	$P_u = 200$ GV	$P_u = 300$ GV
$\beta_{\xi_{\parallel}}$	$A > 0$	0.77 ± 0.07	0.74 ± 0.06	0.75 ± 0.06
	$A < 0$	0.94 ± 0.05	0.84 ± 0.04	0.82 ± 0.04
	mean	0.89 ± 0.05	0.81 ± 0.04	0.79 ± 0.04
$\beta_{\xi_{\perp}}$	$A > 0$	1.65 ± 0.35	2.24 ± 0.34	2.36 ± 0.33
	$A < 0$	1.26 ± 0.14	1.59 ± 0.14	1.70 ± 0.14
	mean	1.35 ± 0.14	1.80 ± 0.13	1.93 ± 0.13
β_{ξ_z}	$A > 0$	4.45 ± 0.61	2.81 ± 0.39	2.45 ± 0.34
	$A < 0$	6.08 ± 0.96	3.82 ± 0.61	3.32 ± 0.53
	mean	5.22 ± 0.55	3.29 ± 0.35	2.86 ± 0.31
$\beta_{G_{ z }}$	$A > 0$	0.48 ± 0.10	0.68 ± 0.09	0.72 ± 0.09
	$A < 0$	0.35 ± 0.05	0.46 ± 0.05	0.49 ± 0.06
	mean	0.39 ± 0.05	0.53 ± 0.05	0.57 ± 0.05
β_{G_r}	$A > 0$	0.85 ± 0.12	0.56 ± 0.08	0.50 ± 0.07
	$A < 0$	0.87 ± 0.13	0.58 ± 0.09	0.52 ± 0.08
	mean	0.86 ± 0.08	0.57 ± 0.05	0.51 ± 0.05
$\beta_{\lambda_{\parallel}}$	$A > 0$	1.00 ± 0.13	1.44 ± 0.18	1.62 ± 0.20
	$A < 0$	1.16 ± 0.15	1.53 ± 0.19	1.65 ± 0.21
	mean	1.08 ± 0.09	1.47 ± 0.12	1.61 ± 0.13

Note. — The β value is the ratio of the parameter derived from MD data at 60 GV to that derived from NM data at 17 GV (see text). Mean β values in $A > 0$ and $A < 0$ epochs and in the total period consisting of all $A > 0$ and $A < 0$ epochs are listed. Mean value and error are deduced from the average and dispersion of

yearly values.

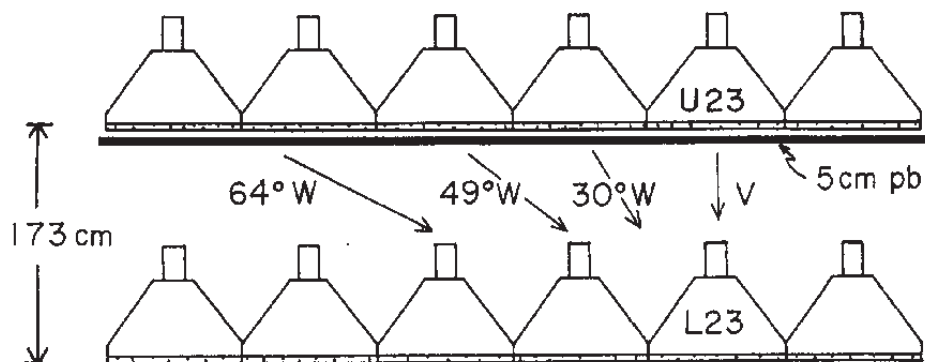


Fig. 1.— Nagoya multi-directional muon detector. This figure is supplied from a document available at the web-site (see text). Nagoya muon detector (MD) consists of two horizontal 6×6 arrays of 1 m^2 unit detectors, vertically separated by 1.73 m, with an intermediate 5 cm layer of lead to absorb the soft component radiation in the air. Each unit detector has a $1 \text{ m} \times 1 \text{ m}$ plastic scintillator viewed by a photomultiplier tube of 12.7 cm diameter. By counting pulses of the twofold coincidences between a pair of detectors on the upper and lower layers, Nagoya MD records the rate of muons from the corresponding incident direction, as shown in this figure. The multi-directional MD comprises various combinations between the upper and lower detectors. The directional channels named “30°W”, “49°W” and “64°W” in this figure correspond to “W”, “W2” and “W3” in Table 1, respectively. The geomagnetic cut-off rigidity (P_c) and median primary rigidity (P_m) in GV are listed in Table 1.

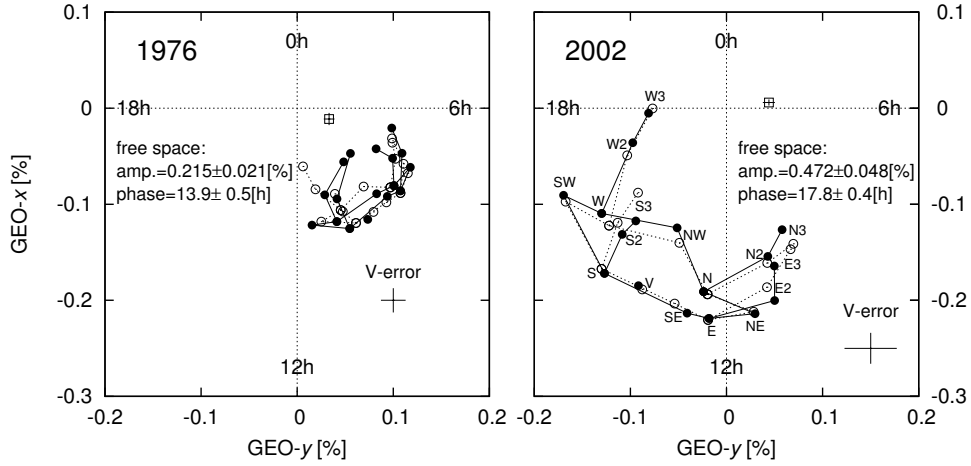


Fig. 2.— Yearly mean harmonic dials of the diurnal anisotropy observed by the Nagoya multi-directional muon detector in 1976 (left) around $A > 0$ solar activity minimum and in 2002 (right) around $A < 0$ solar activity maximum. Solid circles display the harmonic vector $(a_{1,j}^{1,obs}, b_{1,j}^{1,obs})$ observed by the j -th directional channel with $a_{1,j}^{1,obs}$ and $b_{1,j}^{1,obs}$ plotted on the vertical (GEO- x) and horizontal (GEO- y) axes, respectively, while open circles display the best-fit vectors. The phases of the diurnal anisotropy with $x > 0$ and $y = 0$, $x = 0$ and $y > 0$, $x < 0$ and $y = 0$ and $x = 0$ and $y < 0$ are 00:00, 06:00, 12:00, 18:00 hours in the local solar time, respectively. To demonstrate the relative configuration of the observed (best-fit) harmonic vectors in 17 directional channels, the head of each vector is connected with each other by solid (dotted) thin lines (see directional channels indicated in the right panel). An open square with an error cross in each panel displays the common vector representing the atmospheric temperature effect. Amplitude and phase of the best-fit harmonic vector in free space are indicated in each panel. For reference, the cross in the bottom-right corner in each panel represents errors of $a_{1,j}^{1,obs}$ and $b_{1,j}^{1,obs}$ in vertical (V) channel, deduced from the dispersion of monthly values.

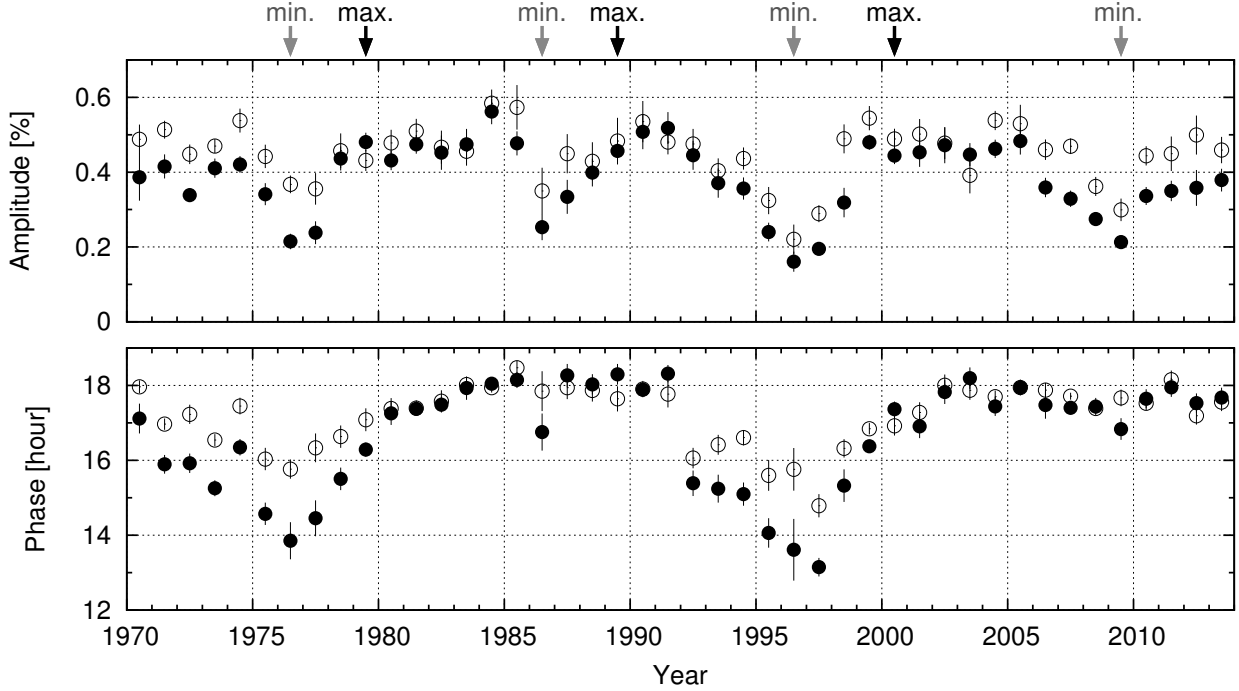


Fig. 3.— Diurnal anisotropy in free-space. Yearly mean amplitude in % and phase (denoted by the local solar time of the maximum intensity in hour) of the diurnal anisotropy are displayed in the upper and lower panels, respectively, each as a function of year on the horizontal axis. The solid and open circles display the anisotropy obtained from MD data at 60 GV and from NM data at 17 GV, respectively (see Table 2 in Appendix A for numerical data from MD). The diurnal anisotropy in this figure is corrected for the Compton-Getting effect arising from the Earth’s orbital motion around the Sun (see text). Yearly mean and error are deduced from the mean and dispersion of monthly values, respectively. The solar maximum and minimum periods are indicated by black and gray arrows above the upper panel, respectively.

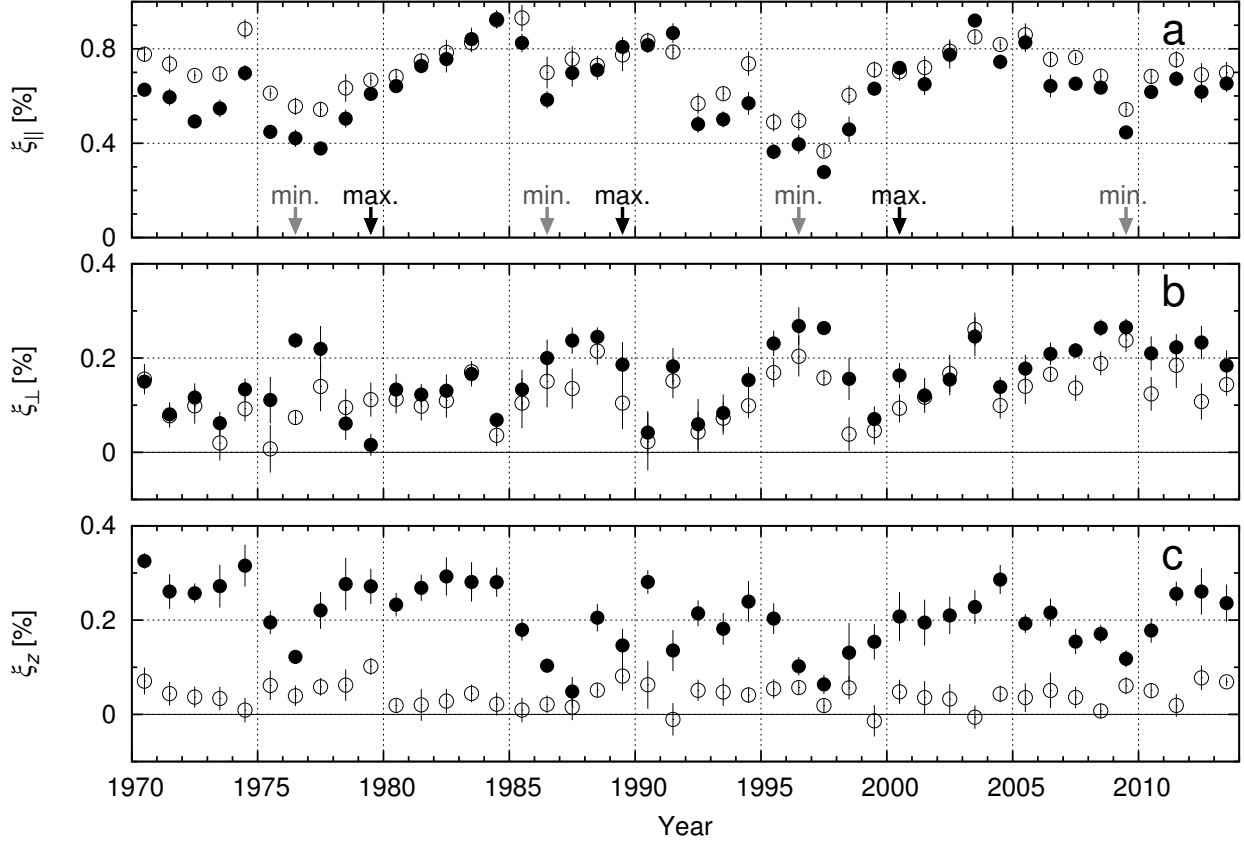


Fig. 4.— Three components of the anisotropy in the solar wind frame. Each panel from top to bottom displays the yearly mean ξ_{\parallel} , ξ_{\perp} and ξ_z in % as a function of year. Solid circles display the anisotropy components derived from MD data at 60 GV, while open circles show the anisotropy derived from NM data at 17 GV (see Table 2 in Appendix A for numerical data from MD). Yearly mean and error are deduced from the mean and dispersion of monthly values, respectively. The solar maximum and minimum periods are indicated by black and gray arrows on the horizontal axis of the top panel, respectively.

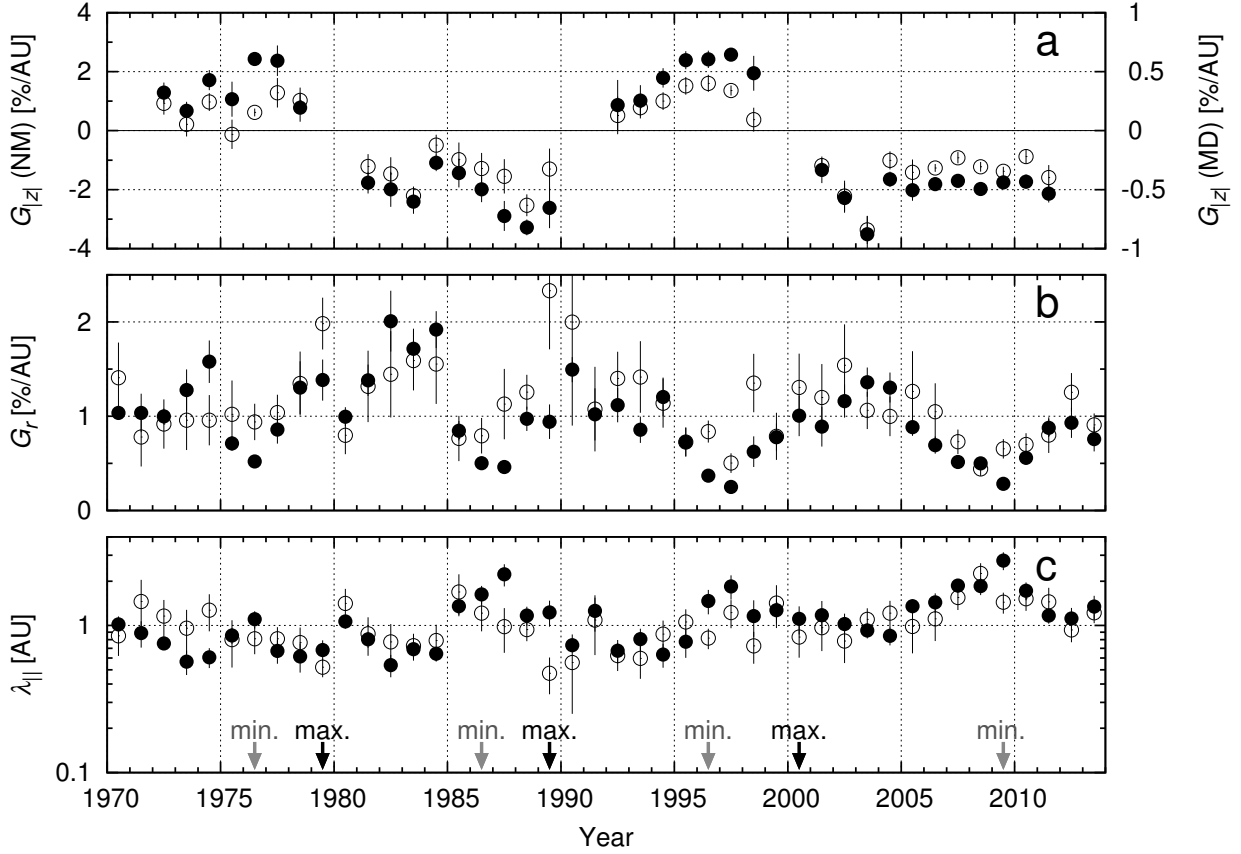


Fig. 5.— Modulation parameters derived from the three dimensional anisotropy. Each panel from top to bottom displays the yearly mean $G_{|z|}$, G_r and $\lambda_{||}$, each as a function of year. Solid circles display parameters derived from MD data at 60 GV, while open circles show parameters derived from NM data at 17 GV (see Table 2 in Appendix A for numerical data from MD). Note that the bidirectional latitudinal density gradient ($G_{|z|}$) in the top panel is defined to be positive (negative) when the spatial distribution of GCR density has a local minimum (maximum) on the HCS. $G_{|z|}$ and G_r in the top and middle panels are plotted on the vertical axis in linear scales, while $\lambda_{||}$ in the bottom panel is plotted in a logarithmic scale. Yearly mean and error are deduced from the mean and dispersion of monthly values, respectively. Because of the definition in equation (21), $G_{|z|}$ is not available in a year when the polarity reversal is in progress. The solar maximum and minimum periods are indicated by black and gray arrows on the horizontal axis of the bottom panel, respectively.

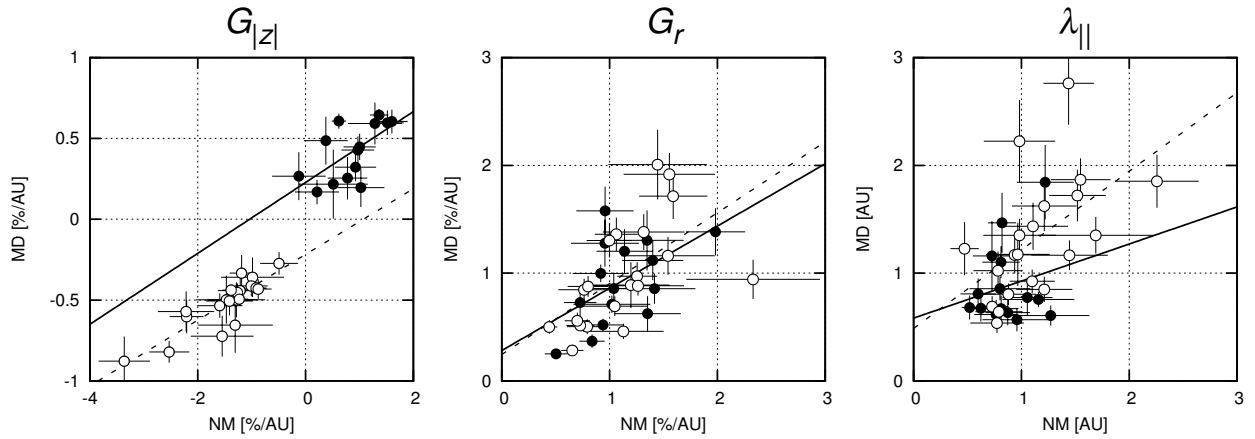


Fig. 6.— Correlation plots between modulation parameters derived from NM data at 17 GV and MD data at 60 GV. The left, middle and right panels show correlations of $G_{|z|}$, G_r and $\lambda_{||}$, respectively. Each panel displays the parameter in figure 5 derived from MD data at 60 GV on the vertical axis as a function of the parameter derived from NM data at 17 GV in the same year on the horizontal axis. Solid and open circles in each panel display parameters in $A > 0$ and $A < 0$ epochs, respectively. Data points in years when the polarity reversal is in progress are omitted in this figure.

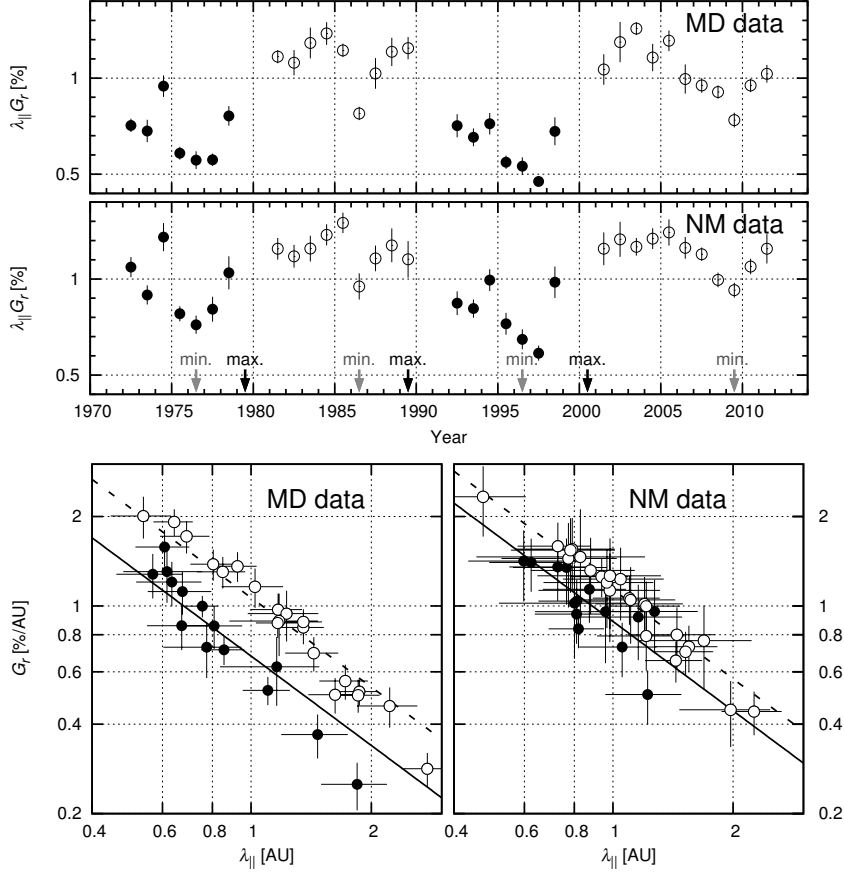


Fig. 7.— Temporal variation of $\lambda_{\parallel} G_r$ and the correlation between G_r and λ_{\parallel} . Upper two panels display yearly mean $\lambda_{\parallel} G_r$ calculated from $\xi_{\parallel}/\cos\psi$, each as a function of year. Top panel shows $\lambda_{\parallel} G_r$ deduced from MD data, while middle panel shows $\lambda_{\parallel} G_r$ deduced from NM data. Yearly mean values in $A > 0$ ($A < 0$) epoch are displayed by solid (open) circles, each with an error deduced from the dispersion of monthly values in each year. Data points in years when the polarity reversal is in progress are omitted in this figure. Bottom two panels are scatter plots between G_r and λ_{\parallel} in logarithmic scales derived from MD data (left) and NM data (right). In each panel, yearly mean G_r on the vertical (y) axis is plotted as a function of λ_{\parallel} on the horizontal (x) axis. Solid and dashed straight lines display the functions $y = c/x$ with a constant parameter c best-fit to data in $A > 0$ and $A < 0$ epochs, respectively. The solar maximum and minimum periods are indicated by black and gray arrows on the horizontal axis of the middle panel, respectively.

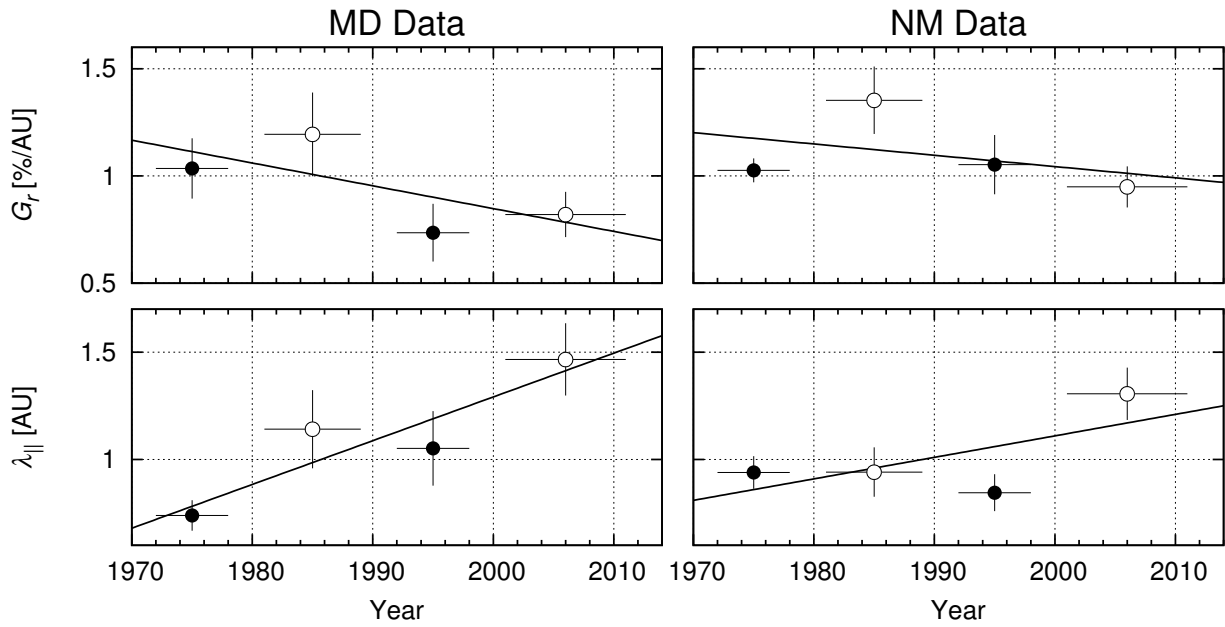


Fig. 8.— Long-term trends of mean G_r and λ_{\parallel} in each solar magnetic polarity epoch. Left (right) two panels display means derived from MD (NM) data. Means in $A > 0$ and $A < 0$ epochs are plotted by solid and open circles, respectively, at the central year of each epoch. The vertical error is deduced from the dispersion of yearly means in each epoch, while the horizontal bar indicates the period included in each epoch. Solid straight line in each panel displays the linear long-term trend best-fit to four data points.

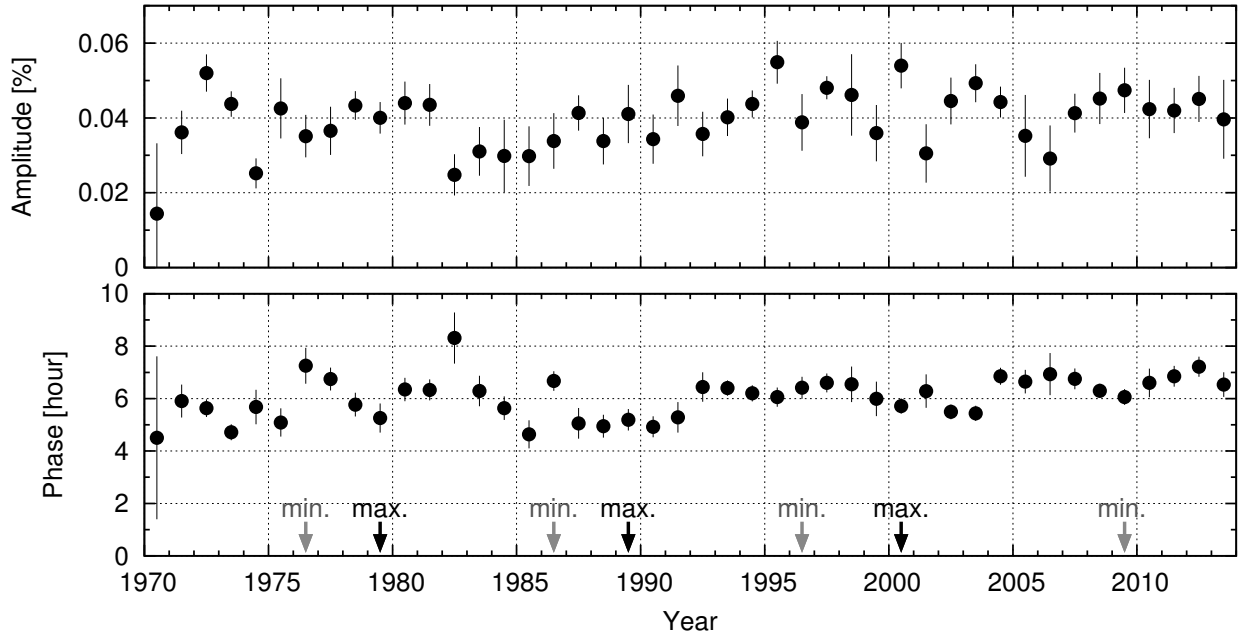


Fig. 9.— Long-term variation of the common vector. Yearly mean amplitude in % and phase (denoted by the local solar time of the maximum intensity) in hour of the common vector are displayed in the upper and lower panels, respectively, each as a function of year on the horizontal axis. The common vector is introduced as a free parameter representing the atmospheric temperature effect on the diurnal anisotropy observed with the MD (see text). Yearly mean and error are deduced from the mean and dispersion of monthly values, respectively. The solar maximum and minimum periods are indicated by black and gray arrows on the horizontal axis of the lower panel, respectively.

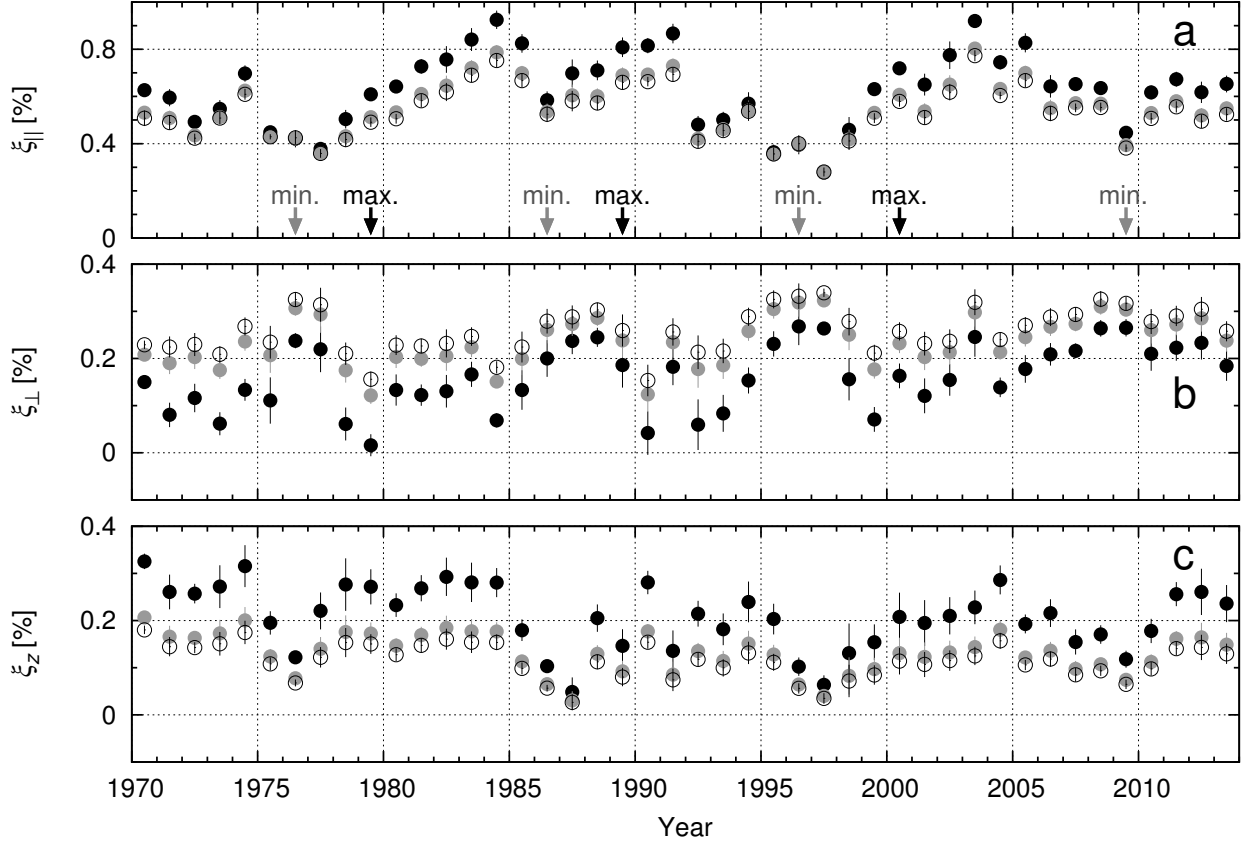


Fig. 10.— Three components of the free-space anisotropy derived from MD data by assuming $P_u = 100, 200, 300$ GV. Solid black, solid gray and open circles represent the components obtained with $P_u = 100, 200, 300$ GV, respectively. The solar maximum and minimum periods are indicated by black and gray arrows on the horizontal axis of the top panel, respectively.